№4, 2021 ISSN 2706-977X

MATERIAL AND MECHANICAL ENGINEERING TECHNOLOGY

Material and Mechanical Engineering Technology | MMET.KZ

Content

Krawiec P., Różański L., Warguła Ł., Domek G., Gutu M., Gavrilin A. Tests and Analysis of the Temperature Distribution of a Flat Belt……3
Kulikov V.Yu., Kvon Sv.S., Chsherbakova Ye.P. Investigation of the Ni-hard Cast Irons Microstructure and Properties after Modification…….....10
Magnucki K., Mielniczuk J., Milecki S. Axisymmetric Bending of a Circular Porous Plate…….....16
Akhmediyev S.K., Filippova T.S., Oryntayeva G.Zh., Donenbaev B.S. Studying Stress-Strain State of Plate with Opening Approximated by Stepwise-Variable Rigidity Rod……...21
Belov N.A. The Joint Effect of Zr and Sc Small Additions on Electrical and Mechanical Properties of Pure Aluminum…….29
Ibatov M.M., Balabaev O.T., Kassymzhanova A.D. Studying the Method of Loading Containers by Testing in the Software Environment……....35

DOI 1052209/2706_977X_2021_4_3 **IRSTI 55.51.33** **UDC 678: 539.376**

Tests and Analysis of the Temperature Distribution of a Flat Belt

Krawiec P.[1], Różański L.[1], Warguła Ł.[1*], Domek G.[2], Gutu M.[3], Gavrilin A.[4]
[1]Poznan University of Technology, Poland,
[2]Kazimierz Wielki University in Bydgoszcz, Poland,
[3]Technical University of Moldova, Moldova,
[4]Tomsk Polytechnic University, Russia
*corresponding author

Annotation. This paper presents thermography as a reliable and fast diagnostic tool for flexible drives. The subject of the research was a flexible connection drive with a NE22 flat belt. These belts are used in machines and equipment that serve driving and transport functions. The dependence of changes in the temperature of the belt and pulleys on the variable load applied with the use of a magnetorheological brake was adopted as the diagnostic characteristic. The ability to ensure the correct and long-term operation of the flexible drives was assessed. It was found that the most favourable operating conditions occur when the temperature values of the driving and slack sides are similar, and the difference between them is stabilised. The conducted tests and analysis of the measurement results indicate the usefulness of thermal imaging diagnostics for the assessment of the thermal state occurring in flexible connection drives under changing loads. The analysis of the test results helped to determine the limits of belt applicability, proper material selection for components and the impact of errors occurring during the manufacture and assembly of the flexible connection drive.

Key words: Flexible connection drive, conveyor belt, driving belt, thermal imaging, diagnostics

Introduction

The first flat belts were made of leather. However, this material was rejected for use as it was not durable enough. At present, a number of belts built on a modern base are covered with leather, as this material is very resistant to abrasion and high temperature. Leather-covered belts work in the toughest applications, such as a wood chipper in wood panel plants. Similarly, in the case of belts operating in difficult environmental conditions, different types of rubber are selected. In closed facilities these are polymers [1, 2], and in the case of huge pressures and very difficult working conditions, steel is used. The conditions related to the operation of the belts are often very complex, the belts dispensing banknotes at ATMs cannot fail, although the environmental conditions between winter and summer vary dramatically. The same is true for belts operating in explosive or chemically aggressive environments. The belt material in cigarette manufacturing systems penetrates into the tobacco and is burned with it, and therefore the range of materials used there is very limited. In modern flat belts, the load-bearing layer is made of materials that provide the least amount of elongation, while maintaining flexibility on small diameter pulleys. A very important feature is resistance to temperature changes and temperature changes of the flexible connection drive. The flat belts currently used in flexible connection drives are made of composite materials with their composition based on plastics. Examples of such applications are conveyors transporting products at high speeds, exposed to significant abrasive wear [3, 4], operating in difficult environmental conditions. In order to assess the surface quality of pulleys and driving belts, optical methods [5, 6], thermography [7, 8], FEM analysis [9, 10] and acoustic methods [11] are increasingly used.

One of the factors behind the increasing use of flat belts is that they can fulfill both driving and transport tasks. The assembly directions for the driving and transport functions are marked on the belts. In the case of long hours of operation of such belts, it is necessary to know and evaluate their thermal state [12-16]. Belt manufacturers provide characteristics for the recommended range of permissible belt temperatures, but the authors of this study decided to conduct a series of experimental tests using a thermal imaging camera to verify these data. The subject of research was a NE22 (Neoprene) flat belt made of a polyester layer and a polychloroprene coating. Such a belt is resistant to abrasion, has a high coefficient of friction, as well as good resistance to oils, greases and ozone. The range of application is -20 to 100°C. The linear speed for which this belt is dedicated can reach 100 m/s. It has antistatic properties and high flexibility. It performs well when working with small diameter pulleys. It is used in high-speed drives, in the textile, paper and other industries.

1. Results and discussion

The ThermaCAM 620 thermal imaging camera manufactured by FLIR (Fig. 1) was used to evaluate the thermal state during operation of the flexible connection drive with flat belts. This device enables measurements with a thermal resolution of 0.05 ºC (i.e. with NETD of 30 ºC). Thermal imaging camera testing is subject to several types of measurement uncertainty.

Fig. 1. - A set for testing heat concentration in a flexible connection drive with a NE22 flat belt

The principle of operation of thermographic systems is to indirectly measure the temperature of the object under test. The primary carrier of information on the temperature of the tested object is the energy luminance of the object's emitted radiation, which after passing through the optical system is converted into an electrical signal in the camera's detection structure. Measuring conditions during industrial testing often differ significantly from calibration conditions. As a result of this divergence, the signal at the detector output is different from the signal under calibration conditions, which increases the uncertainty of the temperature measurement. In order to increase the emissivity of flat-faced pulleys, a chalk spray by HELLING, named Medium No. 3 ENTWICKLER was used. Figure 2 shows the temperature distribution, and Figure 2 shows a thermogram at a rotational speed of 500 rpm and a braking torque load of 1.8 Nm. There is an increase in the average temperature, equal to 27.7 ºC in the driving side and 28.1 ºC in the slack side. Pronounced vibrations of the sides were observed. A slight slippage phenomenon occurred (1.5 rpm). Meanwhile, the recorded average pulley temperatures were equal to 28.6 ºC for the driving side and 28.4 ºC for the slack side.

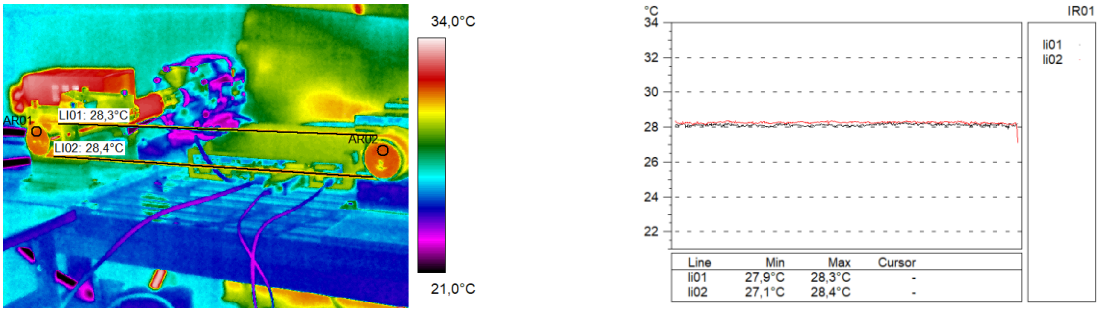

a) b)

Fig. 2. - A thermogram recorded at a rotational speed of 500 rpm and a load (flexible connection drive motion resistance only) of 1.8 Nm (a), profilograms (temperature distributions along lines li01 and li02) recorded at a rotational speed of 500 rpm and a load (flexible connection drive motion resistance only) of 1.8 Nm (red –driving side, black – slack side) (b)

Figure 3a shows the temperature distribution, whereas Figure 3b shows a thermogram at a rotational speed of 1,000 rpm and a braking torque load of 1.8 Nm. The temperature in the driving and slack side was equal and the average temperature stood at 28.1 ºC. No side vibrations were observed.

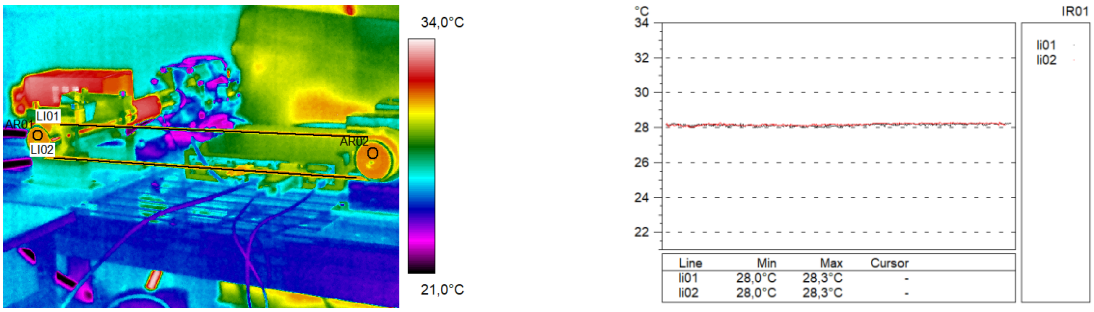

a) b)

Fig. 3. - A thermogram recorded at a rotational speed of 1,000 rpm and a load (flexible connection drive motion resistance only) of 1.8 Nm (a), profilograms (temperature distributions along lines li01 and li02) recorded at a rotational speed of 1,000 rpm and a load (flexible connection drive motion resistance only) of 1.8 Nm (red – driving side, black – slack side) (b)

A slippage phenomenon occurred during testing. The measured speed on the idler pulley was lower than the speed on the drive pulley by 2 rpm. Meanwhile, the recorded average temperatures of the pulleys were equal to 34.6 ºC for the driving side and 33.9 ºC for the slack side.

Figure 4a shows the temperature distribution, whereas Figure 4b shows a thermogram at a rotational speed of 500 rpm and a braking torque load of 5 Nm. The temperature in the driving side was equal to 28.35 ºC and in the slack side it was equal to 28.5 ºC, the slip phenomenon stood at 2.5 rpm.

Meanwhile, the recorded average pulley temperatures were equal to 28.7 ºC for the driving side and 28.6 ºC for the slack side.

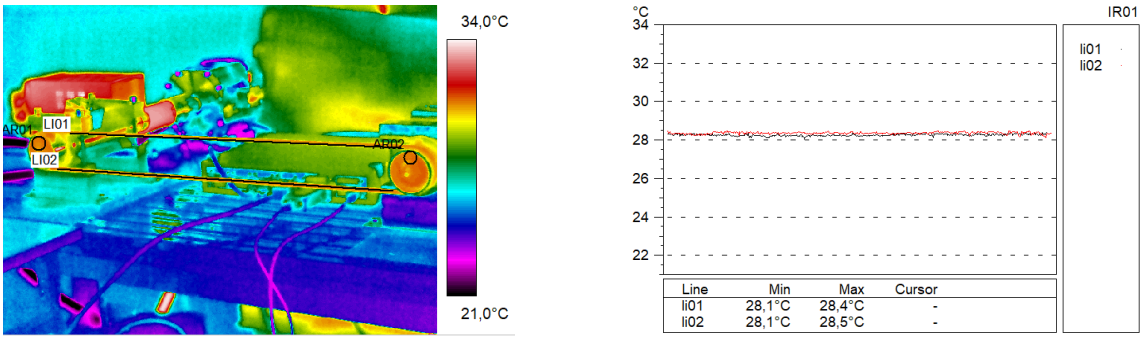

a) b)

Fig. 4 - A thermogram recorded at 1,500 rpm and a load (flexible connection drive motion resistance only) of 1.8 Nm (a), profilograms (temperature distributions along lines li01 and li02) recorded at 1,500 rpm and a load (flexible connection drive motion resistance only) of 1.8 Nm (red – driving side, black – slack side) (b)

Figure 5a shows the temperature distribution, whereas Figure 5b shows a thermogram at a rotational speed of 500 rpm and a braking torque load of 5 Nm. The temperature in the driving side was equal to 28.3 ºC and in the slack side it was equal to 28.5 ºC, a slippage phenomenon of 2.5 rpm was observed.

Meanwhile, the recorded average pulley temperatures were equal to 28.7 ºC for the driving side and 28.6 ºC for the slack side.

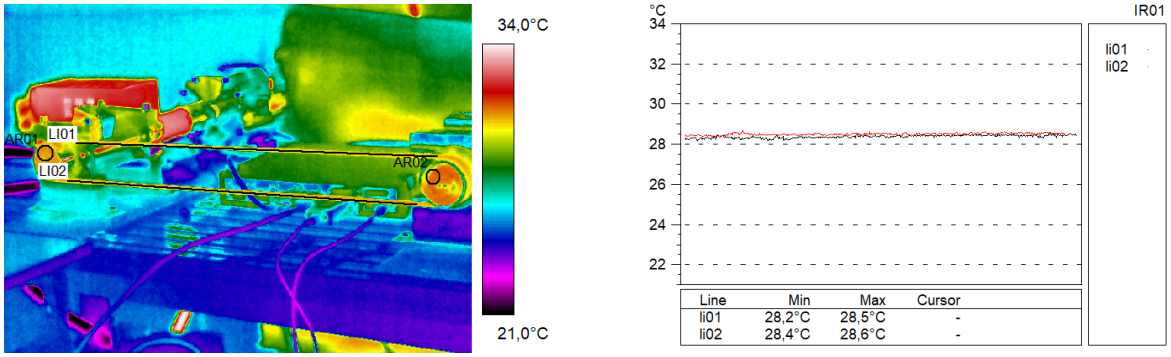

a) b)

Fig. 5. - A thermogram recorded at a rotational speed of 500 rpm and a load (flexible connection drive motion resistance only) of 5 Nm (a), profilograms (temperature distributions along lines li01 and li02) recorded at a rotational speed of 500 rpm and a load (flexible connection drive motion resistance only) of 5 Nm (red – driving side, black – slack side) (b)

Figure 6a shows the temperature distribution, and Figure 6b shows a thermogram at a rotational speed of 1,000 rpm and a braking torque load of 5 Nm. The temperature in the driving side was equal to 28.9 ºC and in the slack side it was equal to 28.8 ºC, the slippage phenomenon stood at 4.8 rpm. Meanwhile, the recorded average temperatures of the pulleys were equal to 29.1 ºC for the driving side and 28.7 ºC for the slack side.

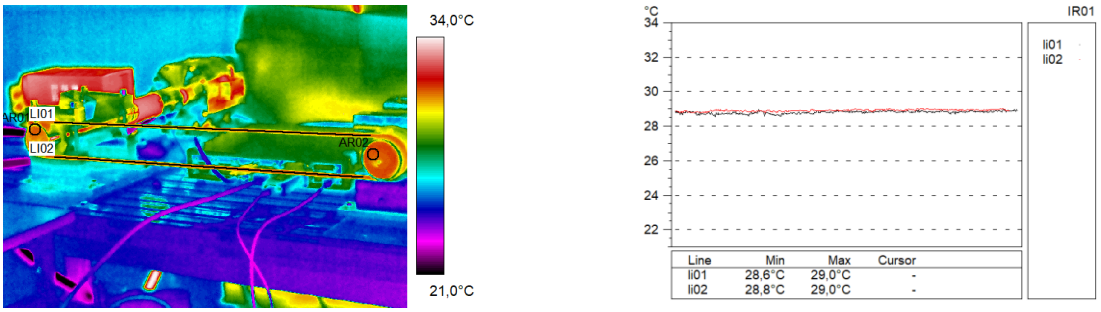

a) b)

Fig. 6. - A thermogram recorded at 1,000 rpm and a load (flexible connection drive motion resistance only) of 5 Nm (a), profilograms (temperature distributions along lines li01 and li02) recorded at 1,000 rpm and load (flexible connection drive motion resistance only) of 5 Nm (red – driving side, black – slack side) (b)

Figure 7a shows the temperature distribution, whereas Figure 7b shows a thermogram at a rotational speed of 1,500 rpm and a braking torque load of 5 Nm. The temperature in the driving side was equal to 29.5 ºC and in the slack side it was equal to 29.4 ºC, the slippage phenomenon totalled 6 rpm. Meanwhile, the recorded average temperatures of the pulleys stood at 29.9 ºC for the driving side and 29.6 ºC for the slack side.

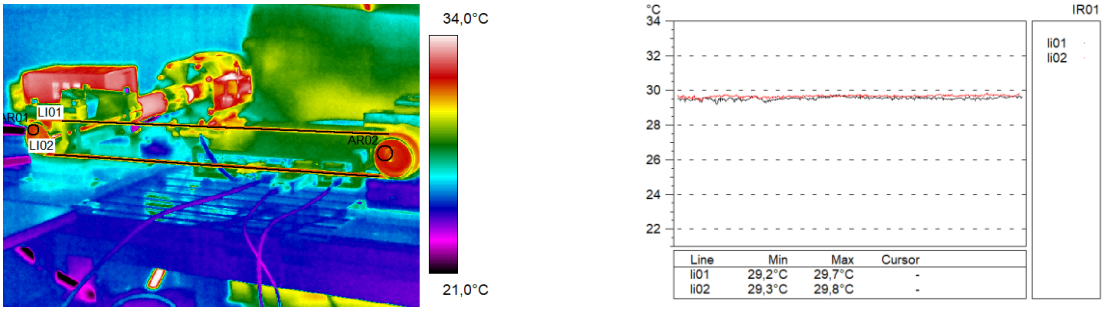

a) b)

Fig. 7. - A thermogram recorded at a rotational speed of 1,500 rpm and a load (flexible connection drive motion resistance only) of 5 Nm (a). Profilograms (temperature distributions along lines li01 and li02) recorded at a rotational speed of 1,500 rpm and a load (flexible connection drive motion resistance only) of 5 Nm (red – driving side, black – slack side) (b)

Figure 8b shows the temperature distribution, whereas Figure 8b shows a thermogram at a rotational speed of 500 rpm and a braking torque load of 7.5 Nm. The temperature in the driving and slack sides was equal to 29.05 ºC, the slippage phenomenon was 2.5 rpm. On the other hand, the recorded average temperature of the pulleys was equal to 29.8 ºC for the driving side and 29.3 ºC for the slack side.

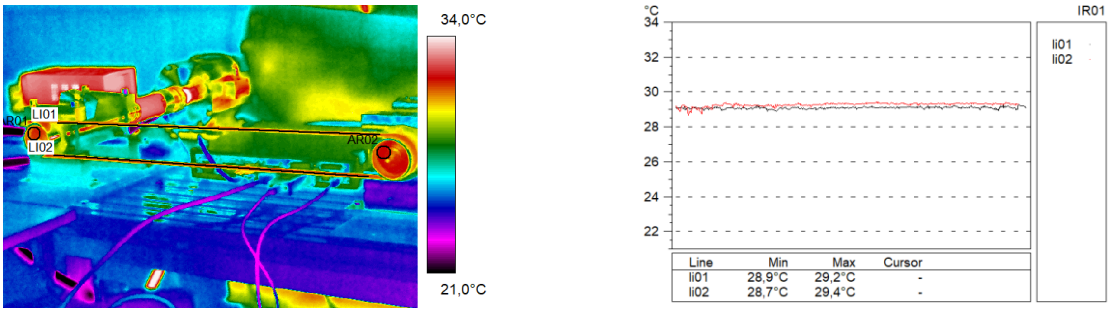

a) b)

Fig. 8. - A thermogram recorded at a rotational speed of 500 rpm and a load (flexible connection drive motion resistance only) of 7.5 Nm (a). Profilograms (temperature distributions along lines li01 and li02) recorded at a rotational speed of 500 rpm and a load (flexible connection drive motion resistance only) of 7.5 Nm (red – driving side, black – slack side) (b)

Figure 9a shows the temperature distribution, whereas Figure 9b shows a thermogram at a rotational speed of 1,000 rpm and a braking torque load of 7.5 Nm. The temperature in the driving side was equal to 30.0 ºC and 29.8 ºC in the slack side. A slippage phenomenon of 6 rpm was recorded. Meanwhile, the recorded average temperatures of the pulleys were practically equal, 28.7 ºC for the driving side and 28.6 ºC for the slack side.

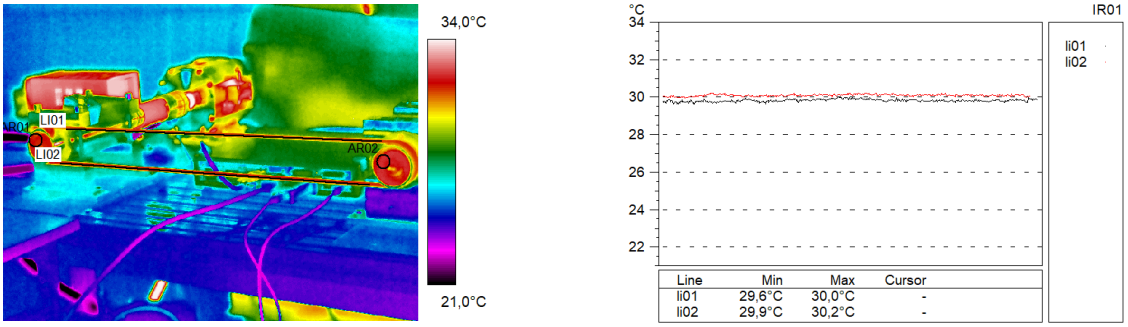

a) b)

Fig. 9. - A thermogram recorded at a rotational speed of 1,000 rpm and a load (flexible connection drive motion resistance only) of 7.5 Nm (a). Profilograms (temperature distributions along lines li01 and li02) recorded at a rotational speed of 1,000 rpm and a load (flexible connection drive motion resistance only) of 7.5 Nm (red – driving side, black – slack side) (b)

Figure 10a shows the temperature distribution, whereas Figure 10b shows a thermogram at a rotational speed of 1,500 rpm and a braking torque load of 7.5 Nm. The temperature in the driving side was equal to 31.1 ºC and in the slack side it was equal to 30.9 ºC. On the idler pulley, the speed was lower by 9 rpm. Meanwhile, the recorded average temperatures of the pulleys were equal to 31.8 ºC for the driving side and 31.2 ºC for the slack side.

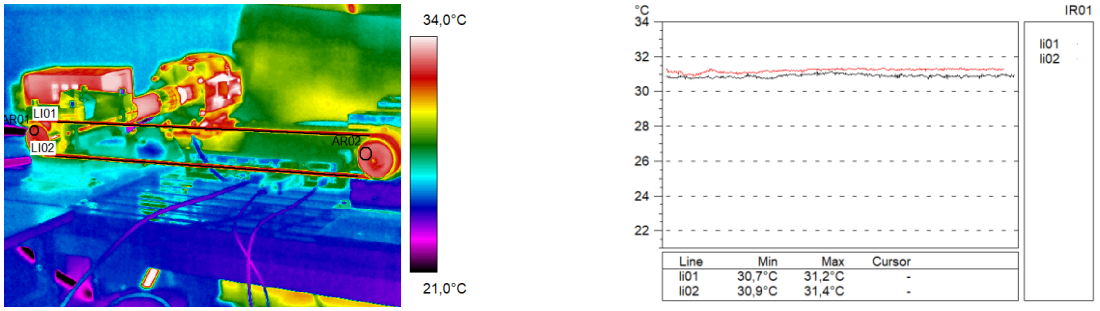

a) b)

Fig. 10. - A thermogram recorded at a rotational speed of 1,500 rpm and a load (flexible connection drive motion resistance only) of 7.5 Nm (a). Profilograms (temperature distributions along lines li01 and li02) recorded at a rotational speed of 1,500 rpm and a load (flexible connection drive motion resistance only) of 7.5 Nm (red – driving side, black – slack side) (b)

Figure 11 shows the characteristics of changes in the temperature of the flexible connection drive equipped with the NE22 belt depending on the changes in the rotational speed of the drive shaft.

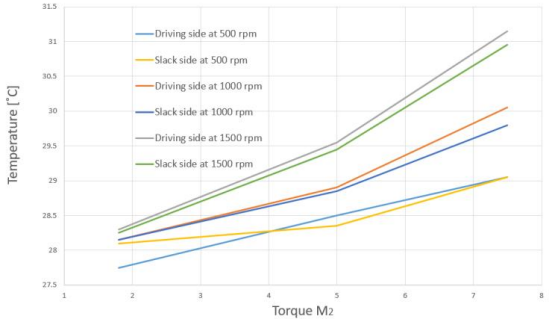

Fig. 11. - Temperature variation in the driving and slack sides for the NE22 belt depending on changes in the rotational speed on the drive shaft

Figure 12 shows the characteristics of the influence of the flexible connection drive load on the temperature in the slack side.

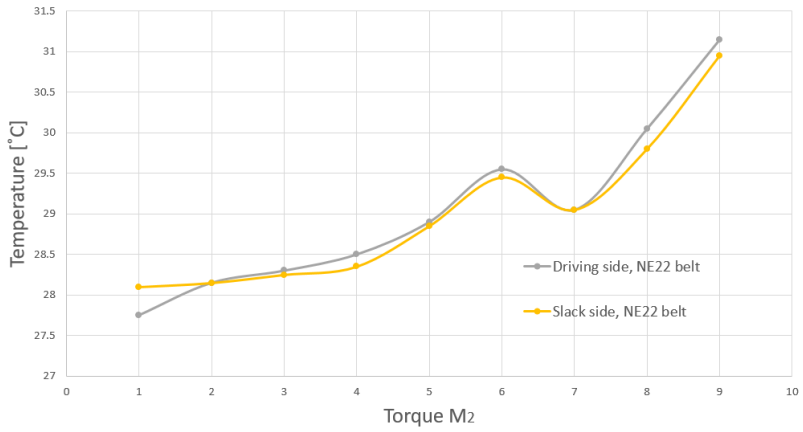

Fig. 12. -Temperature variation in the driving and slack sides for the NE22 belt depending on the torque on the driven shaft

2. Conclusions

This paper presents the results of non-invasive diagnostic tests carried out using a high-end thermal imaging camera.

On the basis of the determined characteristics of the belt temperature dependence on the rotational speed (Fig. 11), it can be concluded that:

1) For the rotational speed of 500 rpm, the temperature difference in the driving and slack side varied from 0.4°C for the minimum load to 0°C for the maximum load;

2) At a load of approx. 4 Nm, the characteristics intersected and from that moment the temperature in the driving side was higher than the temperature in the slack side;

3) For the rotational speed of 1,000 rpm, the temperature difference was initially equal to zero, as the load increased the difference grew and a maximum value of 0.3°C was recorded for the maximum load of 7.8 Nm;

4) For the rotational speed of 1,500 rpm, both the value and temperature difference were stabilised over practically the entire test range from 1.8 Nm – 7.8 Nm;

5) It is worth noting that for a value of about 5 Nm, the temperature characteristics of the driving and slack sides change, with the relation losing its linear character.

Based on Figure 12, it can be concluded that after the flexible connection drive is started and once its operation stabilises, the temperature between the driving and slack sides differs by 0.4°C. The increase in the flexible connection drive load causes the temperature of both sides of the flexible connection drive to increase. The load limit after which the temperature rise occurs is approx. 6 Nm. After exceeding this load, the temperature of the sides drops by about 0.5°C. Then, a linear temperature increase can be observed uniformly in the driving and slack sides. The relatively small differences that arise result from the high elasticity and susceptibility of this belt to vibrations.

The presented results indicate that, taking into account the criterion of correct and long-term operation of flexible drives, the most favourable operating conditions occur when the temperature difference between the driving and slack sides is stabilised and similar to each other.

The determined temperature changes of NE22 type flat belts show a very low temperature influence in comparison to the PU 75A V-belts described in the study [17]. This is due to both the belt materials and the differing, much smaller belt cross-sections.

The conducted experimental studies assessing the thermal state of mechanical devices have confirmed the usefulness of thermography in the diagnosis of the technical condition of a flexible connection drive equipped with a polyurethane thermally welded V-belt, and the obtained results will certainly be useful for the designers and operators of flexible connection drives.

References

[1] Czarnecka-Komorowska D., Wiszumirska K. Sustainability design of plastic packaging for the Circular Economy// “Polimery”, № 65, 2020. - P. 8–17.

[2] Czarnecka-Komorowska D., Wiszumirska K., Garbacz T. Films LDPE/LLDPE made from post-consumer plastic processing structure mechanical properties// “Adv. Sci. Technol. Res. J.” – 2018. No. 12. P 134-142.

[3] Kindrachuk M., Volchenko A., Volchenko D., Volchenko N., Poliakov P., Tisov O., Kornienko A. Polymeres with enhanced energy capacity modified by semiconductor materials// “Funct. Materials” – 2019 No. 26(3) P. 629-634. doi.org/10.15407/fm26.03.629

[4] Ismailov G.M., Tyurin A.E., Gavrilin A.N., Nevinitsyna V.S., Lomovskaya S.A. Study of the identification model of tribological interaction of friction couples// "IOP Conf. Series: Materials Science and Engineering" – 2020 No. 919. 022056. doi:10.1088/1757-899X/919/2/022056
[5] Krawiec P., Waluś K., Warguła Ł., Adamiec J. Wear evaluation of elements of V-belt transmission with the application of optical microscope// "MATEC Web of Conferences", № 157, 2018. - P. 01009-1-8. doi.org/10.1051/matecconf/201815701009.
[6] Krawiec P., Waluś K.J., Warguła Ł., Adamiec J. Wear evaluation study of the multiple grooved pulleys with optical method// "MATEC Web of Conferences", №254, 2019. - P. 01004-1-8. doi.org/ 10.1051/matecconf/201925401004
[7] Krawiec P., Różański L., Czarnecka-Komorowska D., Warguła Ł. Evaluation of the Thermal Stability and Surface Characteristics of Thermoplastic Polyurethane V-Belt// "Materials", № 3(7), 2020. - P. 1502. https://doi.org/10.3390/ma13071502 - 25
[8] Krawiec P., Warguła Ł., Dziechciarz A., Małozięć D., Ondrušová D. Evaluation of chemical compound emissions during thermal decomposition and combustion of V-belts// "Przemysł Chemiczny", 99(1), 2020. - P. 92-98.
[9] Domek G., Wilczyński M. Modelling a timing belt pitch// "MATEC Web of Conferences", № 254, 2019. - P.01011. https://doi.org/10.1051/matecconf/201925401011
[10] Domek G., Kołodziej A., Wilczyński M., Krawiec P. The problem of cooperation of a flat belts with elements of mechatronic systems// "55th International Scientific Conference on Experimental Stress Analysis 2017 EAN", 2017. P. 706-711.
[11] Łazarska M., Woźniak T., Ranachowski Z., Trafarski A., Domek G. Analysis of acoustic emission signals at austempering of steels using neural networks// "Metals and Materials International", № 23(3), 2017. - P. 426-433
Dudek K., Banasiak J., Bieniek J., Diagnosis of kinematic pairs in the rotary mowers// „Maintenance and Reliability", № 20(4), 2003. - P. 17–21
[12] Stawicki T., Sędłak P. Thermal Imaging Studies on Grain Harvester Belt Transmissions// "Diagnostyka", №16(2), 2015. - P. 37-42.
[13] Sundararaman S., Hu J., Chen J., Chandrashekhara K. Temperature dependent fatigue-failure analysis of V-ribbed serpentine belts// "Int. J. Fatigue", №. 31(8), 2019. - P. 1262-1270.
[14] Jia S.S., Song Y.M. Elastic dynamic analysis of synchronous belt drive system using absolute nodal coordinate formulation Nonlinear// "Dynam.", № 81(3), 2015. - P. 1393-1410.
Li W.B., Xin Z.X. Flexural fatigue life prediction of a tooth V-belt made of fiber reinforced rubber// "Int. J. Fatigue", №111, 2018. - P. 269-277.
[15] Krawiec P., Domek G. Transmission gears with V-belts (original text in Polish: Przekładnie cięgnowe z pasami klinowymi). Publishing house: Wydawnictwo Politechniki Poznańskiej – 2019, Poznań, Poland.

Information of the authors

Krawiec Piotr, PhD, institute of machine design, faculty of mechanical engineering of Poznan University of Technology
E-mail: piotr.krawiec@put.poznan.pl

Różański Leszek, associate professor of the faculty of mechanical engineering of Poznan University of Technology
E-mail: leszek.rozanski@put.poznan.pl

Warguła Łukasz, PhD, associate professor of the faculty of mechanical engineering of Poznan University of Technology
E-mail: lukasz.wargula@put.poznan.pl

Domek Grzegorz, PhD, professor of the Faculty of Mechatronics of the Kazimierz Wielki University in Bydgoszcz
E-mail: gdomek@ukw.edu.pl

Gutu Marin, PhD, associate professor of the Department of Mechanical Engineering of the Technical University of Moldova
E-mail: marin.gutu@pmai.utm.md

Gavrilin Alexey, candidate of technical science, associate professor of the mechanical engineering department of Tomsk Polytechnic University
E-mail: gawral@tpu.ru

DOI 1052209/2706_977X_2021_4_10 **IRSTI 53.49.11** **UDC 620.17: 669.131**

Investigation of the Ni-hard Cast Irons Microstructure and Properties after Modification

Kulikov V.Yu., Kvon Sv.S., Chsherbakova Ye.P.*
Karaganda Technical University, Karaganda, Kazakhstan
*corresponding author

Abstract. The research data of modifiers influence on the properties of Ni-hard cast iron are shown in this article. Two types of modifiers were used: mishmetall MC50Fe_3 and complex modifier Spherolite-P. Melting was carried out on a laboratory induction upgraded furnace UIP-25. At the end of the melting, the hardness, wear resistance and the microstructure of the samples were investigated. Studies have shown that data processing with modifiers leads to the appearance of a certain amount of nodular graphite in the structure, which explains the increase in wear resistance with a slight drop in the hardness of the experimental alloys.

Key words: Ni-hard, modifier, wear resistance, hardness, graphite.

Introduction

There are a large number of grades of cast iron on a chromium-nickel basis. The most balanced composition is cast iron of the Ni-hard class. Currently, the term "Ni-hard" is understood as white cast iron on a chromium-nickel basis [1], having high hardness and wear resistance. The chromium content usually does not exceed 9%, and the ratio between silicon and chromium should be strictly maintained within Cr: Si = 2.5:1 in order to avoid the graphitization process [2]. A detailed overview of the effect of alloying elements is given in [1-5]. Table 1 shows the compositions of "classic Ni- hards".

Table 1 - Composition of Ni-hard class cast irons [2]

Element, %	C	Si	Mn	Ni	Cr	S	P	Mo	Cr : Si should be
Ni-hard 1	3-3,6	0,3-0,5	0,3-0,7	3,3-0,8	1,5-2,6	≤0,15	≤0,3	0-0,4	2,5-2,6
Ni-hard 2	≤2,9	0,3-0,5	0,3-0,7	3,3-5,0	1,4-2,4	≤0,15	≤0,3	0-0,4	2,5-2,6
Ni-hard 4	2,6-3,2	1,8-2,0	0,4-0,6	4,5-6,5	8,0-9,0	≤0,15	≤0,3	0-0,4	2,5-2,6

In fact, to date, the possibilities of improving the composition of Ni-hards by simple alloying have almost been exhausted [1,3]. At the same time, new ideas about the mechanisms of wear [4,5] expand the understanding of the properties that are imposed on wear-resistant materials. The global trend of improving wear-resistant materials is the creation of a structure consisting simultaneously of a solid matrix and a relatively soft second phase. The presence of such a structure provides an increase in the coefficient of sliding between the surfaces, and, consequently, reduces the level of wear. For white cast irons, graphite can act as a relatively soft phase. In this case, the partial development of the graphitization process is a necessary condition, which can be regulated by the composition of cast iron [6].

The other wear-resistant cast iron contains by weight%: carbon 2.8-3.5; silicon 0.6-2.0; manganese 0.05-0.5; chromium 2.5-4.5; nickel 3.5-5.0; molybdenum 0.2-0.7; phosphorus 0.5-1.45; sulfur 0.5-0.25; bismuth up to 0.01; iron - the balance [7]. The disadvantage of this cast iron are the low strength, ductility and hardness in the cast state. In this regard, the well-known cast iron does not have the necessary resistance in conditions of impact and abrasive wear.

Wear-resistant cast iron is known, containing (by weight%): carbon - 3-3.7, silicon - 0.5-3; manganese - 0.2-1.5; chromium - 6.8-15; nickel - 4-8; phosphorus - up to 0.4; sulfur - up to 0.15; iron - the balance[8]. The disadvantages of this cast iron are: large linear shrinkage, high values of the elastic modulus and the coefficient of linear expansion.

In article [9], the composition of wear-resistant chromium-nickel cast iron is given, which includes carbon in the amount of 1,3-2,8; chromium -8-14/ %; silicon up to 0.8%; manganese - 4-7%; iron - the balance. However, such a cast iron composition does not provide the necessary wear resistance, especially in modern conditions, when ores with a high content of solid mineral component are subjected to grinding.

The cast iron proposed in [10] additionally includes elements such as boron, vanadium and aluminum. Modification is carried out by cerium and magnesium. The disadvantage of this composition is a rather complex smelting technology associated with the burning of boron and aluminum, as well as the need to modify two types of modifiers.

The composition of cast iron is known [11], in which, in addition to boron, vanadium and aluminum, copper is additionally introduced in order to increase the viscosity of the metal base. The disadvantage of this composition is also the complexity of the smelting technology, since the content of elements such as boron, vanadium and copper is less than 0.5%, which is quite difficult to regulate in industrial conditions.

Wear-resistant cast iron [12] with nodular graphite is well known, containing, by weight%: carbon - 3.6-3.8, silicon - 1.6-2.1, manganese - 0.5-0.7, nickel - 0.8-1.2, molybdenum - 0.5-0.6, chromium - 0.2-0.4, cerium - 0.10-0.16, copper - 0.15-0.30 and iron.

However, this well-known cast iron with nodular graphite in the cast state does not provide the necessary resistance under conditions of impact and abrasive wear. The required properties of the known cast iron are provided only after complex heat treatment (isothermal annealing).

It was shown in [11] that the amount and morphology of the graphite phase in Ni-hards is influenced by the silicon content. As is known, the silicon content must be balanced by a certain chromium content, because otherwise the process of free carbon formation begins. The optimal ratio Cr:Si is 2.5:1, but the silicon content below 0.5% is undesirable, because the fluidity of cast iron decreases and the risk of casting defects increases. Thus, by reducing the ratio between silicon and chromium, it is possible to obtain some free graphite content in the Ni- hard structure. The Yate planning method showed [12] that at a ratio of Cr:Si =1.4:1 graphite inclusions appear in Ni-hard cast iron, and the volume, shape and length of the lamellae largely depend on the ratio Cr:Si. As a quality indicator, the ductility of the matrix was evaluated while maintaining a certain hardness, the best indicators corresponded to.

Thus, when keeping the ratio Cr:Si = 1,4-2,5:1 can obtain a structure with free graphite, but its content will be less than this one shown in [12].

Titanium carbide has a significant influence on the properties of cast iron. One of the trends in improving the properties of Ni-hards is the production of MMC alloys, so-called composites with a metal matrix, which are known as Tinox alloys [2]. Titanium is not present in the composition of classical Ni-hards, however, a number of studies [13-15] consider the effect of the introduction of titanium on the properties of Ni-hards. Titanium forms titanium carbides in Ni-hard, the presence of which increases its hardness and wear resistance. In this paper, it is proposed to introduce titanium carbide, not titanium, as a ligature. Titanium carbides have a high melting point (3140^0C) and do not melt, preserving phase individuality. Due to the low density, titanium carbides float up during casting and are evenly distributed over the casting section. The introduction of titanium carbide into cast iron compensates for the decrease in hardness that occurs as a result of the precipitation of free graphite and a decrease in the volume of chromium carbides. In addition, the introduction of titanium carbide has a beneficial effect on the formation of lamellar graphite during primary crystallization, because it helps to simplify its shape and size, which facilitates, in the future, the process of converting lamellar graphite into nodular[16-18].

In the process of crystallization in Ni-hard with an increased silicon content, lamellar graphite of various morphologies and shapes is formed [7]. However, to increase the complex of wear-resistant properties in the structure, the presence of spherical graphite is necessary [19-21]. For this purpose, a modifier of various nature is introduced - magnesium, complex modifiers based on boron, mishmetall, etc.

1. Materials and the Methods

The next materials were used here: cast iron Ni-hard 2, the composition is shown in table1; ferrosilicon FeSi45 (Si content 41-47wt%, GOST 1415-93); ferrochrome FeCr50C70Si2 (Cr content 45-55wt%, GOST 4757-91); titanium carbide F500 (TU 6-09-492-75); modifier MC50Fe3(Ce content 45-50wt %, TU 48-4-280-91); spherolite-P-complex spheroidizing modifier based on ferrosilicomagnesium with Mg and REM (the composition is a property of LTD “SpheroLite”).

The melting was carried out in an induction laboratory furnace UIP-25 in a corundum crucible, with the air atmosphere. An induction laboratory furnace UIP-25 allows to maintain the temperature up to 2100^0C, the temperature was controlled by a TPP thermocouple (platinum-platinum-rhodium).

The samples for research were discs by the diameter of 80 mm. The wear tests were carried out on a TABER ABRASER 352G device. A tungsten carbide disc was used as an abrasive, the test period was 10,000 cycles. Disk rotation speed equaled 120 rpm. Wear resistance was determined by the relative change in weight:

$$L = M_1/M_2 \times 100\% , \quad (1)$$

where M1 is the mass of the sample after testing

M2 - initial mass of the sample

The hardness was determined on a Wilson VH1156 device,

The microstructure of the samples was examined on the Altami MET-5T microscope, magnification X500. Nital -3 (a 3% solution of HNO_3 in alcohol) was used as a general etchant.

For quantitative metallographic analysis, the Thixomet Pro program was used. The software Thixomet Pro allows solving quantitative problems of metallography, such as determining the number and size of phases and structural components, area and perimeter of phases, size distribution of phases, etc. In particular the software Thixomet Pro is used for the studying the graphite phase, the length of the graphite inclusions, the characteristics of the shape of the inclusions, and the area occupied by the graphite phase. All studies were carried out in at least 3 fields of view.

2. Experimental part

To test these assumptions, the following experiments were carried out. Experimental alloys were smelted in a UIP-25 laboratory furnace with an enhanced cooling system. Ferrosilicon of the FeSi45 brand and ferrochrome of the FeCr50C70Si2 brand were introduced into Ni-hard 2 cast iron to change the silicon and chromium content in the ratio Cr:Si = 1.5-2.5:1. The composition of the charge was calculated according to the generally accepted method and according to the accepted norm of element fumes. The carbon content was controlled prior to the introduction of titanium carbide. Since the introduced titanium carbide already contains carbon, the initial carbon content before alloying with titanium carbide should be 2.3-2.5%. During the casting process (from an intermediate crucible), titanium carbide of the F 500 grade was introduced in an amount of 0.5 - 1.0% fraction - 50 microns. Modification was carried out with mishmetall MC50Fe3 in an amount of 1% by weight. The melts were poured in the temperature range of 1450 – 1460^0C into crucibles shaped as test samples. Table 2 shows the compositions of the experimental alloys, the chemical composition was monitored using a NITONXL2 - 100G and Argon-5CF spectrometer). The finished castings were subjected to the classical Ni-hard 2 treatment - tempering at 250 0C for 2 hours.

Table 2 - Composition of experimental alloys

Sample	Element, %											
	C	Cr	Mn	TiC	Ni	Si	Mo	Cu	Ce	Fe	S	P
1 (with nodular graphite) cast iron	3,6	0,2	0,5	-	1,0	1,8	0,5	0,2	0,1	rest	≤0,05	≤0,09
1/1 (Ni-hard 2)	2,4	2,3	0,6	-	3,3	0,4	0,3	0,1	-	rest	0,1	0,2
2	2,6	1,5	0,6	0,5	4,0	1,5	0,5	0,2	0,1	rest	≤0,05	≤0,09
3	2,8	4,0	0,6	0,8	4,5	2,0	0,5	0,2	0,1	rest	≤0,05	≤0,09
4	3,0	5,0	0,5	1,0	5,0	2,5	0,5	0,2	0,1	rest	≤0,05	≤0,09

Hardness and wear resistance were determined on the samples of experimental alloys (Table 2).

Hardness was determined on a Wilson VH1156 device, for convenience, the results are presented on the Brinell scale. Cast iron of the composition proposed in [2] and Ni-hard 2 were used as samples for comparison. The hardness was determined at least at 5 points, the average results are given. Table 3 shows the test results.

Table 3 - Mechanical properties of prototypes

Number sample	Hardness, HB	Wear resistance, %
1	335	68,2
1/1	550	71,5
2	498	89,9
3	502	92,3
4	523	95,2

As can be seen from the above data, as a result of adjusting the composition of cast iron based on Ni-hard 2 in these ratios, the hardness of the alloy increases by 1.5- 1.6 times compared to the reference sample 1, and the resistance to abrasive wear by 30-35%. In comparison with Ni-hard 2, the hardness drops slightly, but at the same time the wear resistance increases by 20%. A slight decrease in the hardness of the experimental alloys (samples 2-4) compared to Ni-hard 2 is easily explained if we assume that free graphite is present in the structure, which will lead to a decrease in the carbide phase.

Figure 1 shows the structures and an example of using Thixomet Pro software for quantitative metallographic analysis. As can be seen from Figure 1a in the structure of sample No.3 (ratio Cr : Si = 2:1) free graphite of lamellar shape appears in the structure. After modification, graphite acquires a nodular shape, the average size of inclusions is on average 11 microns, the shape factor is about 0.7 (Figure 1a).

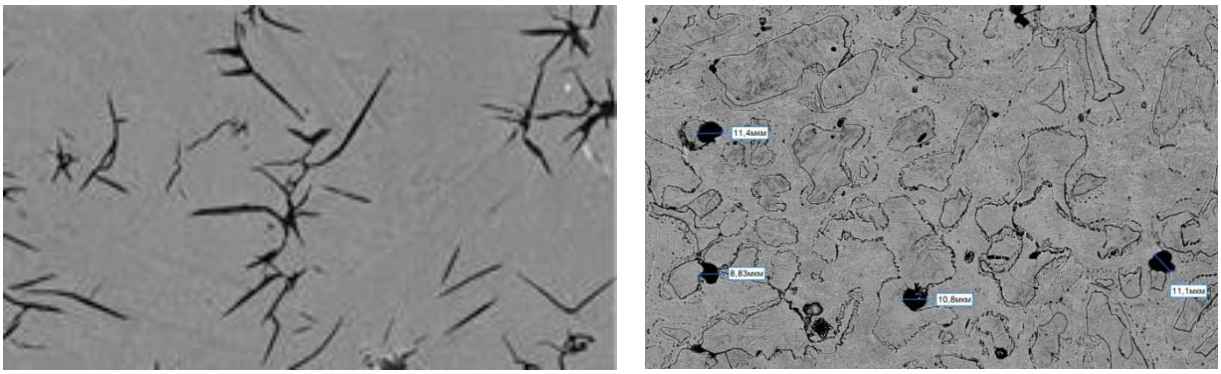

a) b)

Fig. 1. - Microstructure of sample No.3: a - not etched structure, lamellar graphite before modification; b - non-etched structure, nodular graphite before modification) X 500

A comparison of the data in Table 3 and the microstructure analysis makes it possible to establish a clear relationship. Changing the ratio Cr:Si=2:1 in the composition of Ni-hard-2 contributes to the process of graphitization with the formation of lamellar graphite. Further modification contributes to the transformation of graphite into a nodular shape. The presence of nodular graphite in the structure, despite a slight decrease in hardness, has a positive effect on the resistance of the alloy to abrasive wear.

In these studies the $MC50Fe_3$ grade mishmetal was used as a modifier in a standard amount of 0.8 – 1wt. %. Modification with this alloy provided a nodular shape of graphite in cast iron of a given composition in an amount of about 6%. The standard supply of mishmetal in the form of slabs or pyramids necessitates its processing to obtain the necessary dispersion, since in laboratory smelting, the introduction of a modifier in this form is impossible.

It was shown in [4] that the introducing titanium carbide into the composition of chromium-nickel cast irons as a complex ligature leads to some simplifying the shape of lamellar graphite. As a result, the perimeter of the graphite plates decreases, the degree of isometricity and the shape factor increase, which show a tendency to include in a spherical shape. This fact allows us to make assume that in the presence of such a structure, it is possible to use a less effective or a smaller amount of modifier with the result unchanged.

In this study, a complex Spherolite-P modifier based on ferrosilicon with magnesium and a composition of REM with a dispersion of 0.5 - 2mm was used as a modifier. The undoubted advantage of this modifier is its dispersion, which simplifies the technology and modification time compared to the use of mishmetall. The amount of the modifier varied within (0.5 - 1.5 wt. %), the composition of the cast iron remained constant, titanium carbide was introduced into the cast iron before modification. After cooling, the alloy was subjected to conventional heat treatment and then the microstructure (graphite phase), hardness and wear resistance were studied on the samples. Figure 2 and Table 4 show the data obtained. Thixomet Pro software was also used for the analysis. The form factor was calculated using the formula:

$$F = \frac{4A}{\pi D_{max}^2}, \quad (2)$$

where A is the inclusion area

D is the diameter of the inclusion

The shape factor characterizes the tendency to develop a spherical shape of inclusion. In other words, the higher the value of the shape factor, the closer to the spherical shape of this inclusion.

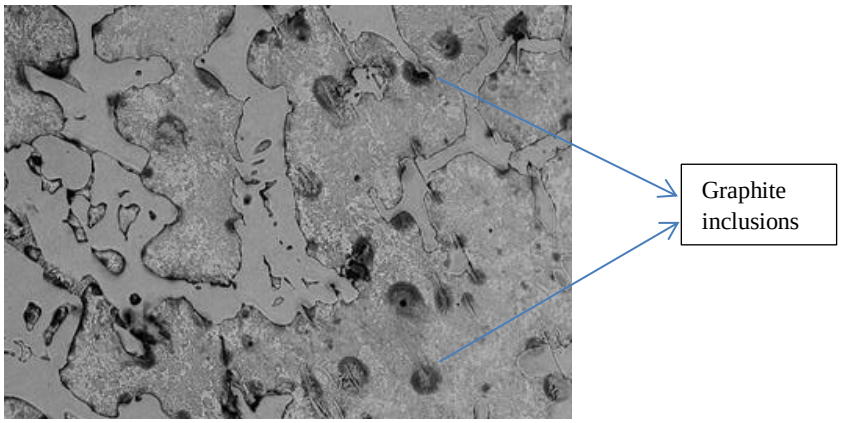

Fig. 2. - Microstructure of cast iron after modification (figure 100): graphite inclusions, X 500

Table 4 - Characteristics of cast iron after modification

№ sample	Amount of Spherolite-P modifier (wt. %)	Average diameter of graphite inclusions, mkm	Inclusion form factor	Hardness, HB	Wear resistance, %
1	0,5	35	0, 90	496	93,5
2	1,0	56	0,92	512	94,7
3	1,5	123	0,93	387	89,2
2	2,0	145	0,938	356	88,3

As can be seen from the data in Table 4, an increase in the amount of modifier above 1% wt,% leads to a significant increase in the average size of graphite, which leads to a decrease in resistance to abrasive wear. This fact is quite easily explained: large graphite inclusions, despite their nodular shape, do not mate well with the matrix and serve as an additional significant source of stress, which leads to a decrease in wear resistance. Based on the data obtained, it can be assumed that the optimal size of graphite inclusions is 35-40 microns, which is provided by the introduction of a modifier in the amount of 0.5%.

3. Conclusions

Thus, it was shown that a decrease ratio Cr:Si is to 2:1 in the base composition of Ni-hard 2 and subsequent treatment with the modifier based on ferrosilicon with magnesium and a composition of REM (Spherolite-P or MC50Fe3) with a dispersion of 0.5 - 2 mm in an amount of 0.5 - 1wt. % leads to the appearance of a certain amount of nodular graphite. The proposed alloy has a lower hardness than Ni-hard-2, but the resistance to abrasive wear increases by 20 - 25%.

References

[1] R&D Report "Development and implementation of technology for the production of Ni- hard-class cast irons with enhanced performance properties for mining and metallurgical equipment parts" for 2020, State Registration № 0118RK00619
[2] https://nickelinstitute.org/media/1728/ni_hardmaterialdataandapplications_11017_.pdf
[3] O.Dogan, J.Hawk, J. Rice// Comparison of Three Ni-Hard I Alloys J. //Materials Science and Technology, Volume 1, 2004/09/01
[4] Jinzhu, Liu, Shizhuo, Li, Yongfa, Man//Wear resistance of Ni-hard 4 and high-chromium cast iron re-evaluated//Wear, Volume 166, Issue 1, 1993. – P. 37-40
[5] K.Thilipkumar, R.Sellamuthu, R.Saravanan// An investigation on the microstructure, wear rate and hardness of Surface alloying Ni-Hard 4 cast iron with Tungsten Using GTA//Materials Today Proceedings, 2020, v. 24, Part 2. - P. 548-556
[6] VK Patent NO, GB No. 2072702 A, United Kingdom
[7] US Patent No. 2662011, cl. 75-128
[8] USSR Patent No. 24537 Composition of wear-resistant cast iron. C22C 37/10. - Publ. 10.09.2006
[9] USSR Patent No. 2234553 Wear-resistant cast iron. C22C 37/10. - Publ. 08/20/2004
[10] RF Patent No. 2384641 Wear-resistant cast iron. S22C 37/04. - Publ. 20.03.2010
[11] A. S. USSR No. 1560605 Wear-resistant cast iron. C22C 37/08. - Publ. 10.08.2004

[12] J. Asensio-Lozandj, J.F. Alvarez-Antolin. Saturated fractional Design of Experiments: toughness and graphite Phase Optimizing in Nihard Cast Irons // J. of materials Eng. and Performance, Volume 17, Issue 20, 2008. - P. 216 - 223.
[13] Branch N and Najafabadi V.N. Investigating the Effect of Titanium Addition on the Microstructure and Mechanical Properties of NH4 Cast Iron Investigating the Effect of Titanium Addition on the Microstructure // Journal of Modern Processes in Manufacturing and Production, 5(1), 2016. – P. 200-204.
[14] Lv.Y, Sun.Y, Zhao.J, Yu.G, Shen.J, and Hu.S. Effect of tungsten on microstructure and properties of high chromium cast iron // Materials and Design, Volume 3, 2012. - P. 303-308.
[15] Mahmoud.E.R.I and El-Labban.H.F. Microstructure and Wear Behavior of TiC Coating Deposited on Spheroidized Graphite Cast Iron Using Laser Surfacing // Engineering, Technology & Applied Science Research. Volume 5, Iss. 4, 2014. - P. 666-701.
[16] Belyakov A.I., Yegorkina N.D., Alekseeva A.P. Production of castings from cast iron with spherical graphite // Procurement production in mechanical engineering, № 2, 2010. - P. 8-13
[17] Osada, H., Kaneta M., Okada K., Ishiyama A.// Effects of chromium content on wear resistance of Ni-hard// cast irons, часть 1//Toraibarojisuto/Journal of Japanese Society of Tribologists, 51 (9), 2006. - P. 603-617
[18] Al-Rubaie, Kassim and Pohl, Michae // Heat treatment and two-body abrasion of Ni-Hard 4 //Wear, №4, 2014. - P.312
[19] Rizov B.L. Some Results from the Investigation of Effects of Heat Treatment on Properties of Ni-Hard Cast Irons// International Journal of Engineering Research and Development,13(2), 2017. – P. 30-35.
[20] Mohammadnezhad M, Javaheri V, Shamanian M, Naseri M, and Bahrami M.//Materials and Design Effects of vanadium addition on microstructure , mechanical properties and wear resistance of Ni-Hard4 white cast iron// Materials and Design, 49, 2013. – P. 888-893.
[21] Branch.N and Najafabadi.V.N. Investigating the Effect of Titanium Addition on the Microstructure and Mechanical Properties of NH4 Cast Iron Investigating the Effect of Titanium Addition on the Microstructure// Journal of Modern Processes in Manufacturing and Production, №5(1), 2016. – P.35-43

Information of the authors

Kulikov Vitaly Yurievich, candidate of technical sciences, professor of the department of nanotechnology and metallurgy of Karaganda Technical University
E-mail: mlpikm@mail.ru

Kvon Svetlana Sergeevna, PhD., professor of the department of nanotechnology and metallurgy of Karaganda Technical University
E-mail: svetlana.1311@mail.ru

Shcherbakova Elena Petrovna, PhD., acting associate professor of the department of nanotechnology and metallurgy of Karaganda Technical University
E-mail: sherbakova_1984@mail.ru

DOI 1052209/2706_977X_2021_4_16 **IRSTI 55.01.05** **UDC 539.3**

Axisymmetric bending of a circular porous plate

Magnucki K., Mielniczuk J., Milecki S.
Łukasiewicz Research Network - Institute of Rail Vehicles TABOR, Poznań, Poland
*corresponding author

Annotation. The subject of the study is bending analysis of the circular porous plate. The analytical model of such a structural element is elaborated. The deflections of the plate for differential boundary conditions are analytically and numerically (FEM) determined and compared. Calculated results for these two methods are presented in tables and figures. *The paper was presented on the 26th International Slovak-Polish Scientific Conference on Machine Modelling and Simulations continues in the Slovak Republic and will be held from 13th to 15th of September 2021 in Bardejovské Kúpele, Slovak Republic.

Key words: porous materials, flexural strength, analytical modeling, modeling with finite element methods.

Introduction

The circular plates are often applicable as machine structures and hence the need for their mechanical modeling. Ventsel and Krauthammer [1] presented in detail theories of circular plates and examples of analytical solutions. Zenkour [2] described shear deformation theory of functionally graded plates. Golmakani [4] performed an analysis of the nonlinear bending of such plates under mechanical and thermal loadings. Mechanical engineering is increasingly using machine parts made of porous materials for example metal foams. Magnucki et al [3] studied analytically and numerically the bending and buckling problems of the rectangular porous plates. In [5] and [6] Magnucki et al considered circular plates with symmetrically varying mechanical properties. Mielniczuk [7] presented in the monograph some considerations on the internal structure and theory of porous media

The subject of the study is the circular porous plate of radius R1 and thickness h with clamped or simply supported edge (Fig.1). The central part of the plate of radius R0 is rigid. The plate is under concentrated force F.

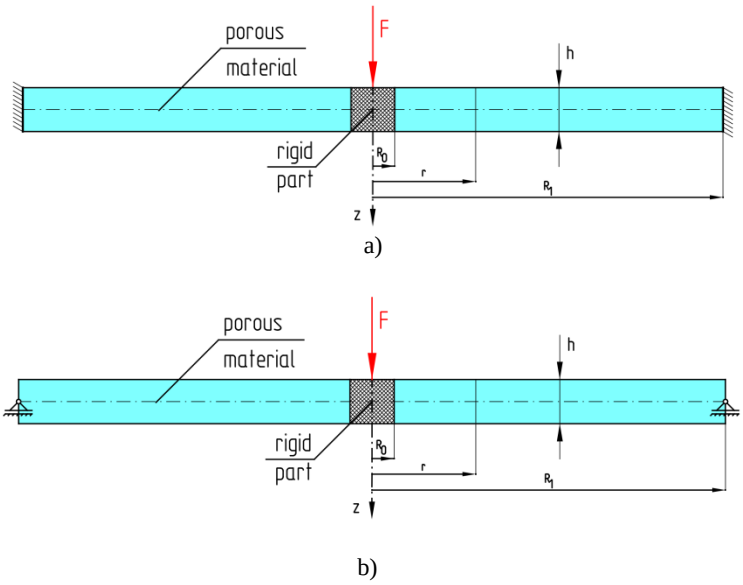

a) clamped edge; b) simply supported edge

Fig.1. - Schemes of the plate with clamped and simply supported edge

The symmetrical variation of the Young's modulus of the porous material in the thickness direction is assumed in the following form:

$$E(\zeta) = E_1 f_e(\zeta) \tag{1}$$

where dimensionless function:

$$f_e(\zeta) = e_0 + 4(1 - e_0)\zeta^2 \tag{2}$$

and: parameter $e_0 = \frac{E_0}{E_1}$ $(0 < e_0 \le 1)$, dimensionless coordinate $\zeta = \frac{z}{h}$ $(-\frac{1}{2} \le \zeta \le \frac{1}{2})$, Young's moduli E_0 for $\zeta = 0$, E_1 for $\zeta = \mp\frac{1}{2}$.

The graph of the function (1) is presented in Fig.2.

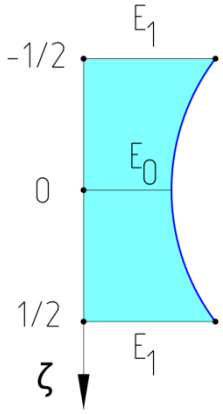

Fig.2. Scheme of the variability of the Young's modulus of porous material

1. Bending of the circular plate – analytical study

1.1 Analytical model

The deformation of the straight normal line after bending of the plate is shown in Fig.3.

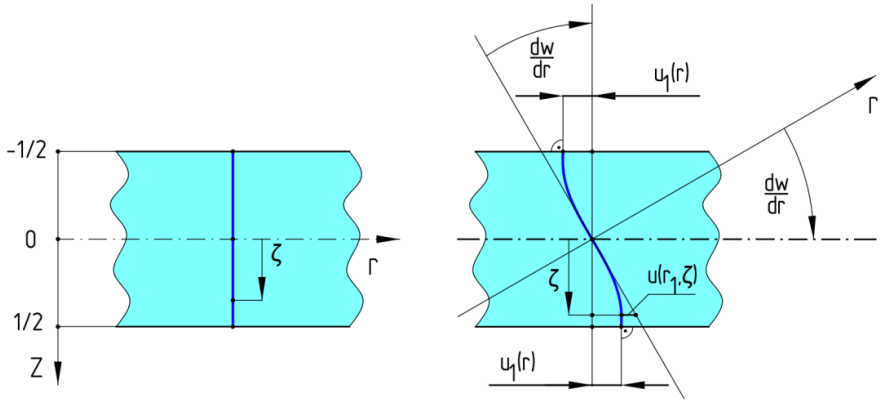

Fig. 3. - The graphical presentation of the deformation of the straight normal line

The radial-longitudinal displacement according to Fig.3 is formulated as follows

$$u(r,\zeta) = -h\left[\zeta\frac{dw}{dr} - f_d(\zeta)\psi(r)\right], \tag{3}$$

where $w(r)$ – deflection, $\psi(r) = u_1(r)/h$ – dimensionless displacement of the points located on the upper and lower surfaces, and the dimensionless function of the deformation of a planar cross section of the straight normal line

$$f_d(\zeta) = \frac{1}{C_0}\int\frac{1-4\zeta^2}{f_e(\zeta)}d\zeta, \tag{4}$$

where $C_0 = \int_0^{1/2}\frac{1-4\zeta^2}{f_e(\zeta)}d\zeta$ – dimensionless coefficient.

Taking into account the paper [5], the radial bending moment:

$$M_r = -D_o\left[C_{ww}\left(\frac{d^2w}{dr^2}+\nu\frac{dw}{rdr}\right)-C_{w\psi}\left(\frac{d\psi}{dr}+\nu\frac{\psi(r)}{r}\right)\right], \tag{5}$$

and the system of two differential equations of equilibrium of the circular plate is as follows:

$$\frac{d}{dr}\left\{\frac{1}{r}\frac{d}{dr}\left[r\left(C_{ww}\frac{dw}{dr}-C_{w\psi}\psi(r)\right)\right]\right\}=\frac{1}{r}\frac{F}{2\pi D_o}, \tag{6}$$

$$\frac{d}{dr}\left\{\frac{1}{r}\frac{d}{dr}\left[r\left(C_{w\psi}\frac{dw}{dr}-C_{\psi\psi}\psi(r)\right)\right]\right\}+\frac{1-\nu}{2}C_{\psi}\frac{\psi(r)}{h^2}=0, \tag{7}$$

where ν – Poisson ratio, $D_o=\frac{E_1h^3}{1-\nu^2}$, and dimensionless coefficients:

$$C_{ww}=\int_{-1/2}^{1/2}\zeta^2 f_e(\zeta)d\zeta,\ C_{w\psi}=\int_{-1/2}^{1/2}f_d(\zeta)f_e(\zeta)\zeta\,d\zeta,\ C_{\psi\psi}=\int_{-1/2}^{1/2}f_d^2(\zeta)f_e(\zeta)d\zeta,\ C_{\psi}=\int_{-1/2}^{1/2}\left(\frac{df_d}{d\zeta}\right)^2 f_e(\zeta)d\zeta.$$

This system of equations (6) and (7) is reduced to one equation in the following form:

$$\left(C_{ww}C_{\psi\psi}-C_{w\psi}^2\right)\frac{d}{dr}\left[\frac{1}{r}\frac{d}{dr}\left(r\psi(r)\right)\right]-\frac{1-\nu}{2}C_{ww}C_{\psi}\frac{\psi(r)}{h^2}=\frac{1}{r}C_{w\psi}\frac{F}{2\pi D_o}. \tag{8}$$

1.2. Bending of the plate with clamped edge

The dimensionless function of the radial-longitudinal displacement is assumed in the form:

$$\psi(\rho)=\left[(1-\rho_0)(1-\rho)-(1-\rho)^2\right]\psi_a, \tag{9}$$

where $\rho_o=\frac{R_0}{R_1}$, and $\rho=\frac{r}{R_1}$ – dimensionless coordinate ($\rho_0\le\rho\le1$).

This function satisfies the following conditions $\psi(\rho_0)=0$ and $\psi(1)=0$. The differential equation (8) is approximately solved with the use of this function (9) and application of the Galerkin method one obtains the coefficient:

$$\psi_a=-\overline{\psi}_a\frac{FR_1}{2\pi D_0}, \tag{10}$$

where $\overline{\psi}_a=\frac{2C_{w\psi}\alpha_0}{2\left(C_{ww}C_{\psi\psi}-C_{w\psi}^2\right)\alpha_1+(1-\nu)C_{ww}C_{\psi}\left(\frac{R_1}{h}\right)^2\alpha_2}$, $\alpha_0=\frac{1}{2}\left(1-\rho_0^2\right)+\rho_0\ln\rho_0$,

$\alpha_1=(1+\rho_0)\alpha_0$, $\alpha_2=\frac{1}{30}(1-\rho_0)^5$.

Therefore, based on the eq. (6) with consideration of the function (9) and conditions $dw/dr\big|_{R_0}=0$, $dw/dr\big|_{R_1}=0$, $w(R_1)=0$, one obtain the maximum deflection of the plate:

$$w_{\max}^{(An)}=w(\rho_0)=\left[\frac{4}{3}(1-\rho_0)^3C_{w\psi}\overline{\psi}_a+1-\rho_0^2-4\frac{(\rho_0\ln\rho_0)^2}{1-\rho_0^2}\right]\frac{FR_1}{16\pi C_{ww}D_0}. \tag{11}$$

The calculations of the exemplary circular plate are carried out for the following data: h=10 mm, R_0=10 mm, R_1=100 mm, E_1=72 GPa, v=0.3. The results of the calculations of the maximum deflection are specified in Table 1.

Table 1 - Maximum deflection – clamped edge

e_0	0.4	0.6	0.8	1.0
$w_{\max}^{(An)}$ [mm]	0.330	0.295	0.268	0.245

1.3 Bending of the plate with simply supported edge

The dimensionless function of the radial-longitudinal displacement is assumed in the form:

$$\psi(\rho)=\left[(1-\rho_0)^2-(1-\rho)^2\right]\psi_a . \tag{12}$$

This function satisfies the following conditions $\psi(\rho_0)=0$ and $d\psi/d\rho|_1=0$. The differential equation (8) is approximately solved with the use of this function (12) and application of the Galerkin method one obtains the coefficient:

$$\psi_a=-\overline{\psi}_a\frac{FR_1}{2\pi D_0}, \tag{13}$$

where $\overline{\psi}_a=\dfrac{2C_{w\psi}\alpha_0}{2\left(C_{ww}C_{\psi\psi}-C_{w\psi}^2\right)\alpha_1+(1-\nu)C_{ww}C_{\psi}\left(\dfrac{R_1}{h}\right)^2\alpha_2}$, $\alpha_0=\dfrac{1}{2}\left(3-4\rho_0+\rho_0^2\right)+(2-\rho_0)\rho_0\ln\rho_0$,

$\alpha_1=2-5\rho_0^2+4\rho_0^3-\rho_0^4+2(2-\rho_0)\rho_0\ln\rho_0$, $\alpha_2=\dfrac{8}{15}(1-\rho_0)^5$.

Therefore, based on the eq. (6) with consideration of the function (12) and conditions $dw/dr|_{R_0}=0$ $M_r(R_1)=0$, $w(R_1)=0$, one obtain the maximum deflection of the plate:

$$w_{\max}^{(An)}=w(\rho_0)=\left[\frac{16}{3}(1-\rho_0)^3C_{w\psi}\overline{\psi}_a+2\left(1-\rho_0^2\right)(1+C_1)+2\left(4C_2+\rho_0^2\right)\ln\rho_0\right]\frac{FR_1}{16\pi C_{ww}D_0}, \tag{14}$$

where $C_1=\dfrac{1}{2}(1-\nu)k_\rho$, $C_2=\dfrac{1}{4}\left[1-(1+\nu)k_\rho\right]$, $k_\rho=\dfrac{1-\rho_0^2(1-\ln\rho_0)}{1+\nu+(1-\nu)\rho_0^2}$.

The calculations of the exemplary circular plate are carried out for the following data: h=10 mm, R_0=10 mm, R_1=100 mm, E_1=72 GPa, v=0.3. The results of the calculations of the maximum deflection are specified in Table 2.

Table 2 - Maximum deflection – simply supported edge

e_0	0.4	0.6	0.8	1.0
$w_{\max}^{(An)}$ [mm]	0.873	0.787	0.717	0.659

2. Bending of the circular plate –numerical (FEM) study

The models of the two porous plates were developed in Abaqus/Standard system. The geometrical and material parameters are the same as in the analytical models. Both models were divided into twenty layers, because of the variability of the Young's modulus. The results of the calculations of the maximum deflection are specified in Table 3 and in the Table 4. In both cases there were applied quadratic hexahedral solid elements.

Table 3 - Maximum deflection – clamped edge

e_0	0.4	0.6	0.8	1.0
$w_{\max}^{(FEM)}$ [mm]	0.337	0.300	0.271	0.248

Table 4 - Maximum deflection – simply supported edge

e_0	0.4	0.6	0.8	1.0
$w_{\max}^{(FEM)}$ [mm]	0.886	0.796	0.723	0.663

3. Conclusions

Maximum difference between deflection obtained as the result of the analytical and numerical study is about 2.1 per cent in the case of clamped edge support and 1.5 per cent in the case of simply supported edge. This difference is caused by the various representation of the Young's modulus in both studies, which is represented by using analytical continuum function in analytical study, and discrete values for each layer in numerical FEM study (Fig.4).

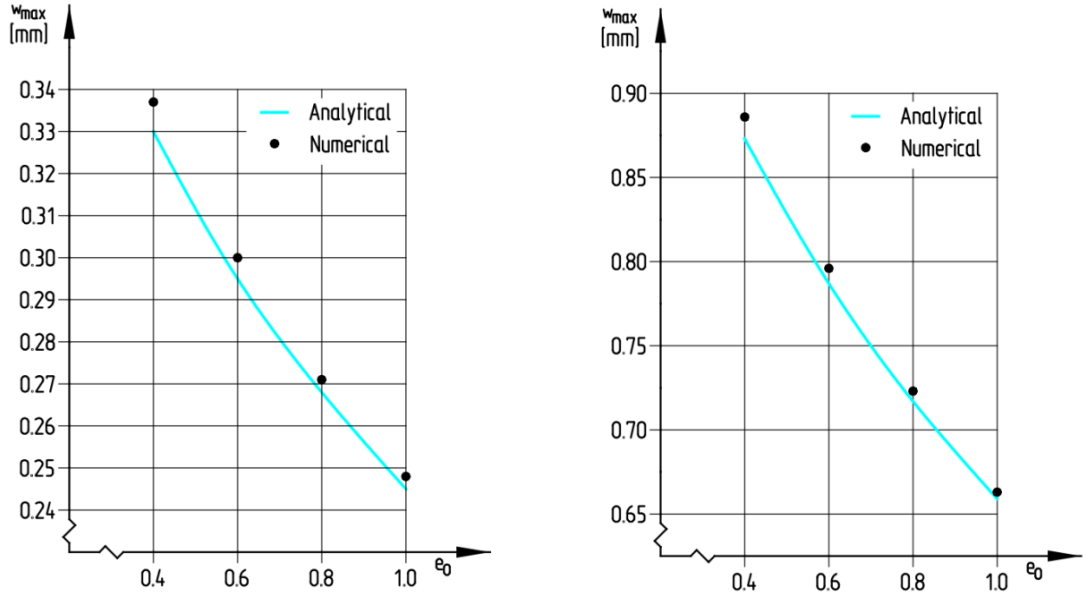

Fig.4. - Graphical comparison of the deflection values calculated analytically and numerically – FEM

References

[1] Ventsel E., Krauthammer T. Thin Plates and Shells. Marcel Dekker Inc., 2001, New York, Basel.
[2] Zenkour A.M. Generalized shear deformation theory for bending analysis of functionally graded plates //Appl. Math. Model, № 30(1), 2006. - P. 67–84.
[3] Magnucki K., Malinowski M., Kasprzak J., Bending and buckling of a rectangular porous plate //Steel Compos. Struct., №6(4), 2006. - P. 319-333.
[4] Golmakani M.E. Nonlinear bending analysis of ring-stiffened functionally graded circular plates under mechanical and thermal loadings //Int. J. Mech. Sci., № 79, 2014. - P. 130–142.
[5] Magnucki K., Stawecki W., Lewinski J., Bending of a circular plate with symmetrically thickness-wise varying mechanical properties //Steel Compos. Struct., № 34(6), 2020. - P. 795-802.
[6] Magnucka-Blandzi E., Magnucki K., Stawecki W., Bending and buckling of a circular plate with symmetrically varying mechanical properties //Appl. Math. Model., №89(2), 2021. - P. 1198-1205.
[7] Mielniczuk J. Plasicity of porous materials //Wydawnictwo Politechniki Poznańskiej, Poznań 2000.

Information of the authors

Magnucki Krzysztof , Phd, associate professor Łukasiewicz Research Network - Institute of Rail Vehicles TABOR
E-mail: krzysztof .magnucki@tabor.com.pl

Mielniczuk Janusz, Phd, Professor, Łukasiewicz Research Network - Institute of Rail Vehicles TABOR
E-mail: janusz.mielniczuk@put.poznan.pl

Milecki Szymon, Phd, associate professor, Łukasiewicz Research Network - Institute of Rail Vehicles TABOR
E-mail: szymon. milecki@tabor.com.pl

DOI 1052209/2706_977X_2021_4_21 IRSTI 55.13.95 UDC 739.384.001.5

Studying Stress-Strain State of Plate with Opening Approximated by Stepwise-variable Rigidity Rod

Akhmediyev S.K., Filippova T.S.*, Oryntayeva G.Zh., Donenbaev B.S.
Karaganda Technical University, Karaganda, Kazakhstan
*corresponding author

Abstract. In the paper there is considered a study of stress-strain state of a rectangular wall panel with an opening for a window aperture (Figure 1). The design scheme of a real wall panel is represented in the form of a hinge-supported at the ends, stepwise-variable-thickness rod. Similar designs are also used in mechanical engineering as metal parts with an opening. The design of such a rod is performed for a vertical concentrated load P_x (weight of the overlying wall panels of 2-5 floors) and for the effect of various loads in the form of a uniformly distributed transverse pressure q_y. The opening for the window aperture is accounted through the moments of inertia of the rod parts cross sections that are given along the length of the rod. As a result of the calculations performed along the length of the stepwise-variable rod, there have been obtained ordinates of the transverse and angular displacements, axial displacements, internal transverse and longitudinal forces, and the corresponding diagrams of the force and strain factors have been plotted according to their values.

Keywords: stress-strain state, metal plate with an opening, stepwise-variable rigidity rod, differential equation of a curved axis, vertical and horizontal loads, numerical approximation, grid method, displacements, internal power factors, power parameters diagrams.

Introduction

When designing bearing enclosing structures of large-panel housing constructions, as well as parts of machine-building facilities, there arise the problems of their durability, rigidity, and stability. The task is complicated by the fact that wall structures with an opening of various sizes and shapes represent a multiply connected region of mechanics of a rigid strained body.

Some attempts to solve such a problem with known analytical methods face serious mathematical problems; Therefore the use of numerical methods, in particular the grid method [1-4], is relevant. Numerical approximation permits to obtain a solution of this problem in the finite (closed) form.

Thus, solving this problem by the numerical method of grids made it possible to study operation of a rectangular panel with an opening, i.e. to solve the issue of their strength, rigidity, and stability for their safe operation.

The results obtained can be used for designing plates and panels with openings under arbitrary load, with various geometric and design parameters that is topical of machines and mechanisms.

1. Methodology of numerical study

In the process of erecting a large-panel apartment house wall panels are joined to each other on the surface of the building facades with horizontal and vertical stitches, through which vertical (q_y) and horizontal (q_x) uniformly distributed loads caused by the self-weight of the panels and coatings, as well as caused by the impact of wind loads are transmitted onto the panel. In the same way, when designing machines and mechanisms, parts with a with an opening are used.

According to the design features, the conditions of supporting wall panels and machine parts, current loading schemes (Figure 1) can be approximated by various methods of operation of the said structure (panel).

Later on, taking into account the fact that the thickness and specific weight of the insulation (soft rockwool) is negligible, and ignoring the presence of a layer of insulation, a wall panel is considered as a homogeneous (single-layer) structure.

The constructive solution of panels with an opening, from the viewpoint of mechanics of a rigid strained body are homogeneous plate with a technological with an opening (Figure 1).

The original differential equation of the fourth order for a compressed-curved axis of the rod of variable cross-section [1] has been solved by the numerical method of finite differences using a uniform linear grid with the number of divisions n=8. In the finite differences there are also recorded the boundary conditions by which there are excluded deflections of "contour" and "out-of-contour" grid nodes.

As a result of numerical approximation the original differential equation is replaced with a system of linear algebraic equations (SLAE) that is solved by methods known in mathematics.

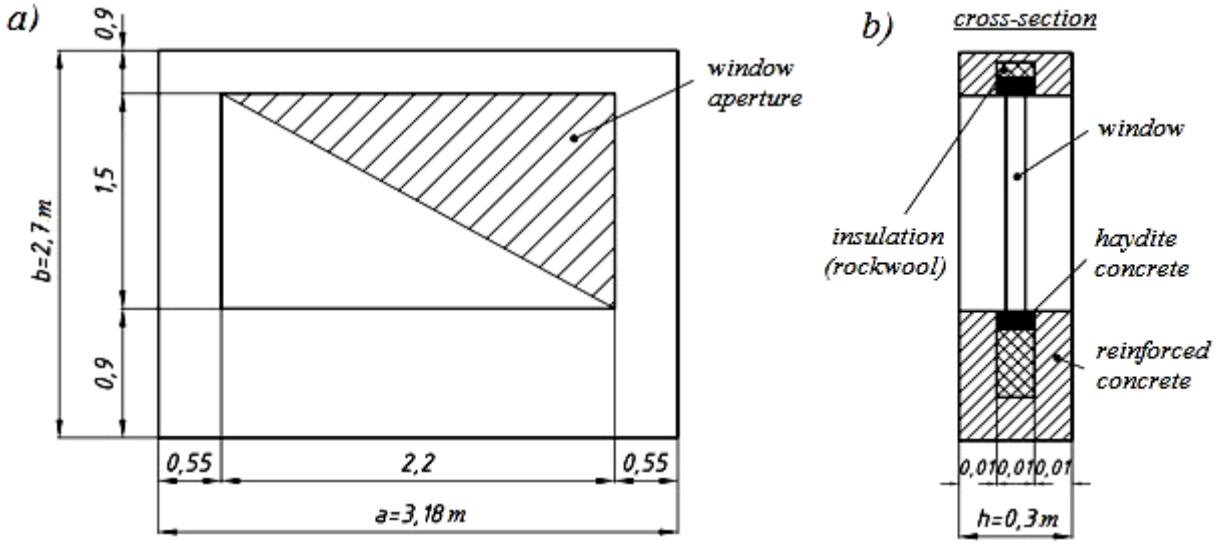

Fig. 1. - Geometrical and structural design of a plate with a plate with an opening

In this paper we approximate the original two-dimensional (flat) panel (Figure 1) as a rod (one-dimensional) structure taking into account the presence of a technological opening aperture with dimensions (2.2x1.5 m). As a result, we obtain the following design diagram (Figure 2).

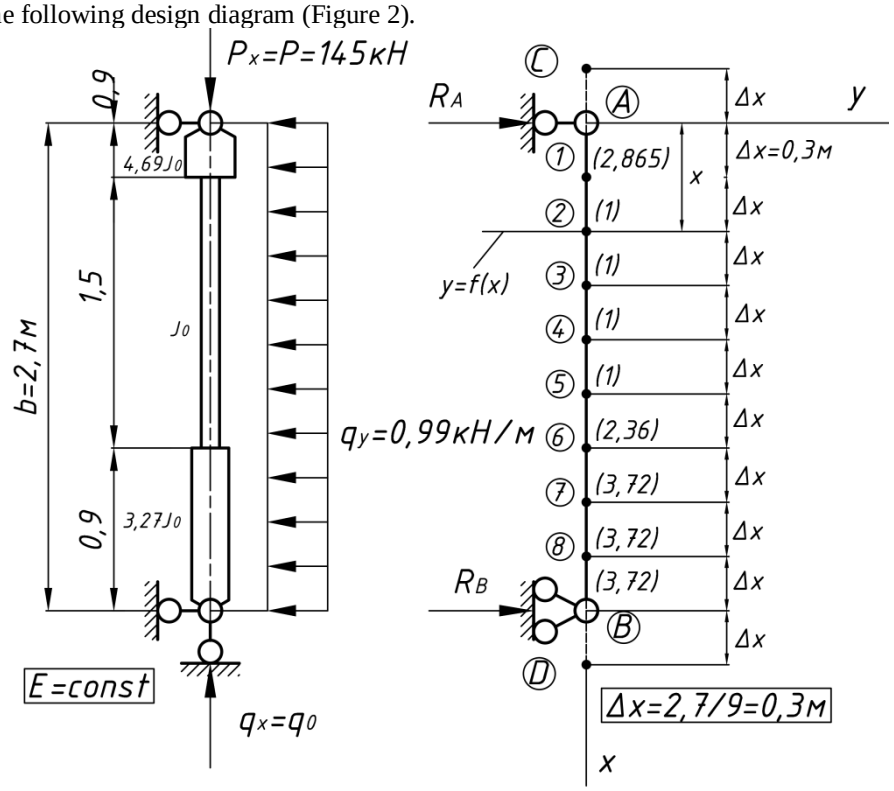

Fig. 2. - Design diagram in the form of an equivalent rod of a variable-cross section

The moments of inertia of the rod sections taking into account the initial dimensions of the plate (panel) (Figure 1) will have a stepwise variable dependence, at this:

$$J_0 = J_{XC,B} = 0{,}3914m^4$$

The load values q_y are calculated by [1, 2]:

$$\omega_m = \omega_0 \cdot k \cdot c \quad (1)$$

where $\omega_0 = 0{,}48\ kPa\ (48\ kg/m^2)$ is rated transverse load;

$k = 0.65$ [5];

$c = 1.2$ [6];

$\nu_f = 1.3$ is the coefficient of reliability for load [5].

The calculated load (per 1 m^2) according to (1) is:

$$\omega = \omega_m \cdot \nu_f = 0{,}48 \cdot 1{,}3 = 0{,}624 kPa;$$

$$\omega = 0.624 kPa = 62.4 kg/m^2.$$

The linear load (per 1 l.m.) (according to Figure 1) is:

$$q_y = \omega \cdot (3{,}18) = 0{,}624 \cdot 0{,}624 = 2{,}370 kN/m, \text{ i.e.}$$

$$q_y = 2.370 kN/m = 237.2 kg/m.$$

Calculating the P_x (P) (for the panel in question)

Concentrated force $P_x = P = 14\ t$ (along the panel plane) is:

$$P_x = P = 14\ t = 143\ kN.$$

The material of the plates is low-carbon steel C235.

Calculating the moments of inertia of the plate (panel) parts.

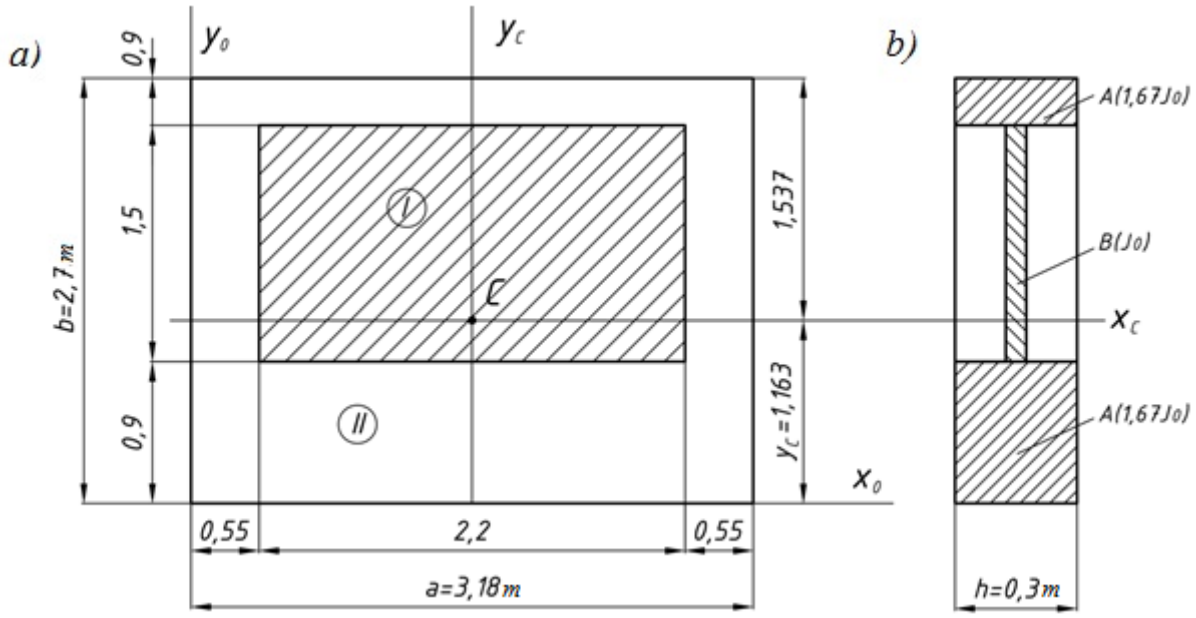

Fig. 3. - Plate (panel) design parameters

a) for the entire panel

$$J_{XC} = \left(\frac{bh^3}{12}\right)_{II} - \left(\frac{bh^3}{12}\right)_{I} = \frac{3{,}18 \cdot (2{,}7)^3}{12} - \frac{2{,}2 \cdot (1{,}5)^3}{12} = 5{,}216 - 0{,}619 = 4{,}597;$$

$$J_{XC} = 4{,}597 m^4;$$

$$J_{YC} = \left(\frac{hb^3}{12}\right)_{II} - \left(\frac{hb^3}{12}\right)_{I} = \frac{2{,}7 \cdot (3{,}18)^3}{12} - \frac{1{,}5 \cdot (2{,}2)^3}{12} = 7{,}235 - 1{,}331 = 5{,}904;$$

$$J_{YC} = 5{,}904 m^4.$$

b) for the panel parts

$$J_{XC,A} = 3{,}18 \cdot 0{,}3 \cdot (1{,}537 - 0{,}15)^2 = 0{,}954 \cdot 1{,}924 = 1{,}835 m^4;$$

$$J_{XC,B} = 2\cdot\left(0{,}55\cdot 1{,}5\cdot(0{,}487)^2\right) = 2\cdot(0{,}825\cdot 0{,}2372) = 0{,}3914 m^4;$$

$$J_{XC,C} = 3{,}18\cdot 0{,}9\cdot(0{,}713)^2 = 1{,}455 m^4;$$

$$J_{XC,B} = 0{,}3914 m^4 = J_0;\ \ J_{XC,A} = 1{,}875\frac{0{,}3914}{0{,}3914} = \frac{1{,}875}{0{,}3914}J_0 = 4{,}69 J_0;$$

$$J_{XC,B} = J_0;\ \ J_{XC,A} = 4{,}69 J_0;$$

$$A = 3{,}18\cdot 2{,}7 - 2{,}2\cdot 1{,}5 = 8{,}586 - 3{,}3 = 5{,}286 m^2;$$

$$A = 5{,}286 m^2.$$

$$y_C = \frac{S_{x_0}}{A} = \frac{3{,}18\cdot 2{,}7\cdot 1{,}35 - 2{,}2\cdot 1{,}5\cdot 1{,}65}{5{,}286} = \frac{11{,}5911 - 5{,}445}{5{,}286} = 1{,}163 m.$$

y_C=1,163 m is the coordinate of the center of gravity of the wall panel with an opening relative to the X_0 axis (Figure 3).

The differential equation of the compressed-curved rod equilibrium has the form [6]:

$$\left[EJ(x)y''\right] + \left[N(x)y'\right] = P(y) \tag{2}$$

or the expanded form:

$$EJy^{IV} + 2EJ'y^{III} + \left(EJ'' + N\right)y^{II} + N^I y^I = P(y) \tag{3}$$

At the $N = const$ load we have:

$$EJy^{IV} + 2EJ'y^{III} + EJ''y^{II} + N^I y^I = P(y) \tag{4}$$

To implement equation (4) we use the finite difference method [1, 3, 4].

The design diagram of a compressed-curved rod of stepwise-variable rigidity with which help there is modeled (approximated) a plate with an opening (Figure 1) operation is shown in Figure 2.

The values of deflections in the contour and out-of-contour lines of the linear grid (Figure 2) taking into account fastening of the beam ends:

$$y_A = 0;\ \ y_B = 0;\ \ y_C = -y_1;\ \ y_D = -y_7 \tag{5}$$

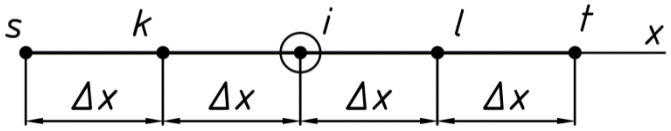

Fig. 4. - A fragment of the linear grid region

Let us write down equations (4) into the finite-difference expressions of the derivatives in equation (4) [2, 3] for the *i*-th node of the linear-grid region (Figure 4) taking into account the boundary conditions (5). The number of calculated nodes of the grid n=7 (Figure 2). As a result, we obtain a system of linear algebraic equations (SLAE) of the 8th order (Table 1).

$$y^{IV} + 2\frac{J'}{J_0}y^{III} + \frac{J''}{J_0}y^{II} + N\frac{y''}{EJ_0} = \frac{P(y)}{EJ_0} \tag{6}$$

$$\frac{6y_i - 4(y_k + y_l) + (y_s + y_t)}{\Delta x^4} + \frac{1}{J_0}\cdot\frac{J_l - J_k}{4(\Delta x^4)}\left[-2(y_l - y_k) + (y_t - y_s)\right] +$$

$$+ \frac{1}{\Delta x^4}\cdot\frac{1}{J_0}\left[-2J_i + (J_k + J_l)\right]\left[-2y_i + (y_k + y_l)\right] + \frac{N}{EJ_0}\cdot\frac{1}{\Delta x^4}\left[-2y_i + (y_k + y_l)\right]$$

From here:

$$y_i\left\{6-2\left[\frac{-2J_i}{J_0}+\frac{(J_k+J_l)}{J_0}\right]-\frac{2N\Delta x^2}{EJ_0}\right\}+y_k\left\{-4+\frac{(J_l-J_k)}{J_0}+\left[\frac{-2J_i}{J_0}+\right.\right.$$

$$\left.\left.+\frac{(J_k+J_l)}{J_0}\right]+\frac{N\Delta x^2}{EJ_0}\right\}+y_l\left\{-4-\frac{(J_l-J_k)}{J_0}+\left[\frac{-2J_i}{J_0}+\frac{(J_k+J_l)}{J_0}\right]+\right.$$

$$\left.+\frac{N\Delta x^2}{EJ_0}\right\}+y_s\left\{\left[1-\frac{(J_l-J_k)}{4J_0}\right]+y_t\left[1+\frac{(J_l-J_k)}{4J_0}\right]\right\}=\frac{P(y)\Delta x^4}{EJ_0};$$

$$a_1y_i+a_2y_k+a_3y_l+a_4y_s+a_5y_t=\frac{P(y)\Delta x^4}{EJ_0}, \quad (7)$$

where

$$\left.\begin{gathered} a_1=6-2(-2\alpha_i+\alpha_k+\alpha_l)-\frac{2N\Delta x^2}{EJ_0}; \\ a_2=-4+0{,}5(\alpha_l-\alpha_k)-2\alpha_i+\alpha_k+\alpha_l+\frac{2N\Delta x^2}{EJ_0}; \\ a_3=-4-0{,}5(\alpha_l-\alpha_k)-2\alpha_i+\alpha_k+\alpha_l+\frac{2N\Delta x^2}{EJ_0}; \\ a_4=1-0{,}25\alpha_l+0{,}25\alpha_k,\ \ a_5=1+0{,}25\alpha_l-0{,}25\alpha_k; \\ a_i=J_i/J_0,\ \ a_k=J_k/J_0,\ \ a_l=J_l/J_0. \end{gathered}\right\} \quad (8)$$

In Figure 2:

$$\alpha_{A_1}=4{,}69,\ \ \alpha_{1_1}=0{,}5(1+4{,}69)=2{,}865,\ \ \alpha_{2_1}=\alpha_{3_1}=\alpha_{4_1}=1,$$

$$\alpha_{5_1}=2{,}36,\ \ \alpha_{6_1}=\alpha_{7_1}=\alpha_{B_1}=3{,}72,\ \ \Delta x=l/9.$$

$P=P_1=P_2=...=P_8=q_y\dfrac{\Delta x^4}{EJ_0}$ is load at the grid nodes. (9)

The system of linear algebraic equations (SLAE) recorded according equation (7) has the form:

$$A\cdot\vec{y}=\vec{P}, \quad (10)$$

where A is the square matrix of the 8th order (Table 1);

y= | {y1,y2,…,y8} | is the vector of angular displacements (Figure 2);

P= | {P1,P2,…,P8} | is the vector of the right part taking into account the load specified in Figure 2.

The impact of the transverse load according to (9) is:

$$P_y=\frac{2{,}57\cdot0{,}0081}{2\cdot10^7\cdot0{,}3914}=2{,}45\cdot10^{-9},\ \ P_y=2{,}45\cdot10^{-9},$$

The impact of the longitudinal load is:

$$P_x=\frac{N\Delta x^2}{EJ_0}=\frac{q_x\cdot\Delta x^2}{EJ_0}=\frac{143\cdot0{,}09}{2\cdot10^7\cdot0{,}3914}=1{,}644\cdot10^{-6},\ \ P_x=1{,}644\cdot10^{-6},$$

The "*A"* matrix (formula 10) for the rod presented in Figure 2 in the general (in alphabetic form) has the form (Table 1).

Next there are calculated the coefficients (8) for the rod in Figure 2.

The "*A*" matrix (in numerical form) taking into account the calculations by expressions (8), is given in Table 2.

The results of solving the SLAE task using the standard MatCAD program are shown in Figure 5. Here: 5,a is the design diagram of the rod; 5,b is the diagram of transverse displacements y_i; 5,c is the diagram of the angles the cross sections of rotation θ_i; 5,d is the diagram of displacements z_i; 5,e is the diagram of bending moments M_{xi}; 5,f is the diagram of transverse forces Q_{yi}; 5,g is the diagram of longitudinal forces N_i.

Table 1 - Resolving finite-difference system of equations SLAE (alphabetic matrix "A")

№	y_1	y_2	y_3	y_4	y_5	y_6	y_7	y_8	Right part, m
1	a_{11}-a_{41}	a_{31}	a_{51}						$2{,}45\cdot10^{-9}$
2	a_{22}	a_{12}	a_{32}	a_{52}					$2{,}45\cdot10^{-9}$
3	a_{43}	a_{23}	a_{13}	a_{33}	a_{53}				$2{,}45\cdot10^{-9}$
4		a_{44}	a_{24}	a_{14}	a_{34}	a_{54}			$2{,}45\cdot10^{-9}$
5			a_{45}	a_{25}	a_{15}	a_{35}	a_{55}		$2{,}45\cdot10^{-9}$
6				a_{46}	a_{26}	a_{16}	a_{36}	a_{56}	$2{,}45\cdot10^{-9}$
7					a_{47}	a_{27}	a_{17}	a_{37}	$2{,}45\cdot10^{-9}$
8						a_{48}	a_{28}	a_{18}-y_{58}	$2{,}45\cdot10^{-9}$

Then, on the basis of the known formulas of strength of materials [2, 7], there are determined normal and tangential stresses along the normal areas of the rod cross-section, according to which there are calculated reduced stresses which makes it possible to estimate strength, rigidity and stability of the given wall panel (Figure 1).

Calculating the coefficients according to expression (8):

$$a_{11} = 6 - 2\left(-2\cdot 2{,}285 + 4{,}69 + 1\right) - 2\cdot 1{,}644\cdot 10^{-6} = 6 - 2\left(-5{,}73 + 5{,}69\right) - $$
$$- 3{,}288\cdot 10^{-6} = 6{,}08 - 3{,}288\cdot 10^{-6};$$
$$a_{21} = \left[-4 + 0{,}5\left(1 - 4{,}69\right) - 2\cdot 2{,}865 + 1 + 4{,}69\right] + 1{,}644\cdot 10^{-6} = \left(-4 - 1{,}845 - \right.$$
$$\left. - 5{,}73 + 5{,}69\right) + 1{,}644\cdot 10^{-6} = -5{,}885 + 1{,}644\cdot 10^{-6};$$
$$a_{31} = \left[-4 - 0{,}5\left(1 - 4{,}69\right) - 2\cdot 2{,}865 + 1 + 4{,}69\right] + 1{,}644\cdot 10^{-6} = \left(-4 + 1{,}845 - \right.$$
$$\left. - 5{,}73 + 5{,}69\right) + 1{,}644\cdot 10^{-6} = -2{,}155 + 1{,}644\cdot 10^{-6};$$
$$a_{41} = 1 - 0{,}25\cdot 1 + 0{,}25\cdot 4{,}69 = 1 - 0{,}25 + 1{,}1725 = 1{,}923;$$
$$a_{51} = 1 + 0{,}25\cdot 1 - 0{,}25\cdot 4{,}69 = 1 + 0{,}25 - 1{,}1725 = 0{,}0078;$$
$$a_{12} = 6 - 2\left(-2\cdot 1 + 2{,}285 + 1\right) - 2\cdot 1{,}644\cdot 10^{-6} = 2{,}27 - 3{,}288\cdot 10^{-6};$$
$$a_{22} = -4 + 0{,}5\left(1 - 2{,}865\right) - 2\cdot 1 + \left(2{,}865 + 1\right) + 1{,}644\cdot 10^{-6} = -4 - 0{,}9325 - 2 + $$
$$+ 3{,}865 + 1{,}644\cdot 10^{-6} = -3{,}068 + 1{,}644\cdot 10^{-6};$$

Table 2 - Numerical matrix "A" (for designing stepwise-variable cross section (analog of the wall panel))

№	y_1	y_2	y_3	y_4	y_5	y_6	y_7	y_8	Right part, m
1	$4.157-3.288\cdot10^{-6}$	$-2.195+1.644\cdot10^{-6}$	0.0078						$2.45\cdot10^{-9}$
2	$-3.068-1.644\cdot10^{-6}$	$2.27-3.288\cdot10^{-6}$	$-1.208+1.644\cdot10^{-6}$	5..338					$2.45\cdot10^{-9}$
3	1.000	$-4+1.644\cdot10^{-6}$	$6-3.288\cdot10^{-6}$	$-4+1.644\cdot10^{-6}$	1.000				$2.45\cdot10^{-9}$
4		1.000	$-4+1.644\cdot10^{-6}$	$6-3.288\cdot10^{-6}$	$-4+1.644\cdot10^{-6}$	1.000			$2.45\cdot10^{-9}$
5			0.660	$-1.96+1.644\cdot10^{-6}$	$_6$ $3.28-3.288\cdot10^{-}$	$-3.32+1.644\cdot10^{-6}$	1.340		$2.45\cdot10^{-9}$
6				0.3195	$-2.64+1.644\cdot10^{-6}$	$6-3.288\cdot10^{-6}$	$-5.36+1.644\cdot10^{-6}$	1.6805	$2.45\cdot10^{-9}$
7					0.660	$-4.68+1.644\cdot10^{-6}$	$8.72-3.288\cdot10^{-6}$	$-6.04+1.644\cdot10^{-6}$	$2.45\cdot10^{-9}$
8						1.000	$-4+1.644\cdot10^{-6}$	$5-3.288\cdot10^{-6}$	$2.45\cdot10^{-9}$

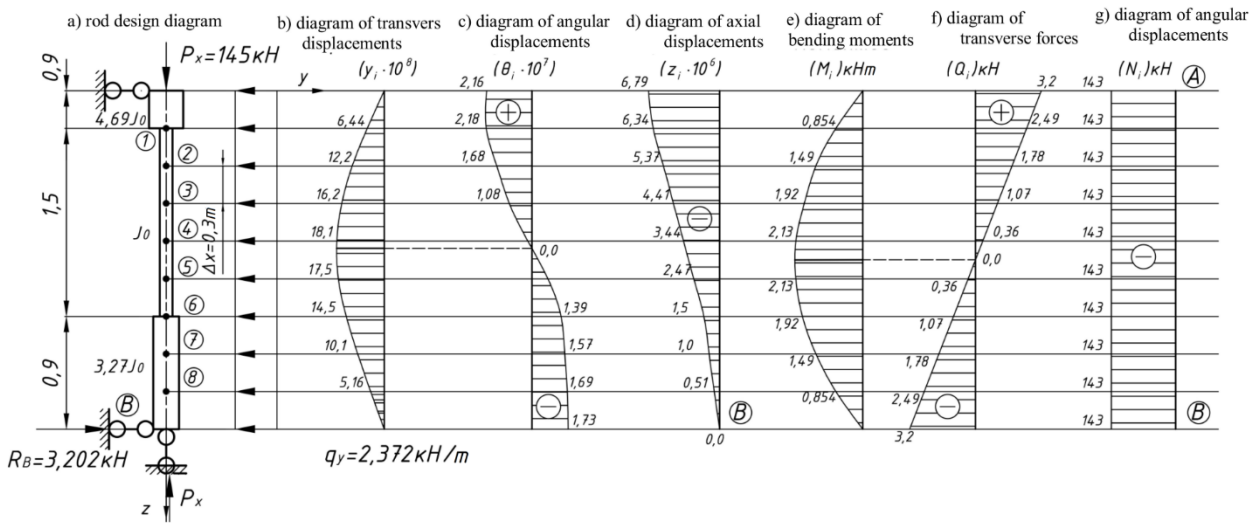

Fig. 5. - Results of solving the SLAE task using the standard MatCAD program

$$a_{32} = -4 - 0{,}5(1 - 2{,}865) - 2 \cdot 1 + (2{,}865 + 1) + 1{,}644 \cdot 10^{-6} = -4 + 0{,}9325 +$$
$$+ 1{,}865 + 1{,}644 \cdot 10^{-6} = -1{,}203 + 1{,}644 \cdot 10^{-6};$$
$$a_{42} = 1 - 0{,}25 \cdot 1 + 0{,}25 \cdot 2{,}865 = 1 - 0{,}25 + 0{,}71625 = 1{,}4663;$$
$$a_{52} = 1 + 0{,}25 \cdot 1 - 0{,}25 \cdot 2{,}865 = 1 + 0{,}25 - 0{,}71625 = 05338;$$
$$a_{13} = 6 - 2(-2 \cdot 1 + 1 + 1) - 2 \cdot 1{,}644 \cdot 10^{-6} = 6 - 3{,}288 \cdot 10^{-6};$$
$$a_{23} = -4 + 0{,}5(1 - 1) - 2 \cdot 1 + 1 + 1 + 1{,}644 \cdot 10^{-6} = -4 + 1{,}644 \cdot 10^{-6};$$
$$a_{33} = -4 - 0{,}5(1 - 1) - 2 \cdot 1 + 1 + 1 + 1{,}644 \cdot 10^{-6} = -4 + 1{,}644 \cdot 10^{-6};$$
$$a_{43} = 1 - 0{,}25 \cdot 1 + 0{,}25 \cdot 1 = 1; \quad a_{53} = 1 + 0{,}25 \cdot 1 - 0{,}25 \cdot 1 = 1;$$
$$a_{14} = 6 - 2(-2 \cdot 1 + 1 + 1) - 2 \cdot 1{,}644 \cdot 10^{-6} = 6 - 3{,}288 \cdot 10^{-6};$$
$$a_{24} = -4 + 0{,}5(1 - 1) - 2 \cdot 1 + 1 + 1 + 1{,}644 \cdot 10^{-6} = -4 + 1{,}644 \cdot 10^{-6};$$
$$a_{34} = -4 - 0{,}5(1 - 1) - 2 \cdot 1 + 1 + 1 + 1{,}644 \cdot 10^{-6} = -4 + 1{,}644 \cdot 10^{-6};$$
$$a_{44} = 1 - 0{,}25 \cdot 1 + 0{,}25 \cdot 1 = 1; \quad a_{54} = 1 + 0{,}25 \cdot 1 - 0{,}25 \cdot 1 = 1;$$
$$a_{15} = 6 - 2(-2 \cdot 1 + 1 + 2{,}36) - 2 \cdot 1{,}644 \cdot 10^{-6} = 3{,}28 - 3{,}288 \cdot 10^{-6};$$
$$a_{25} = -4 + 0{,}5(2{,}36 - 1) - 2 \cdot 1 + 1 + 2{,}36 + 1{,}644 \cdot 10^{-6} = -1{,}96 + 1{,}644 \cdot 10^{-6};$$
$$a_{35} = -4 + 0{,}5(2{,}36 - 1) - 2 \cdot 1 + 1 + 2{,}36 + 1{,}644 \cdot 10^{-6} = -4 - 0{,}68 + 1{,}36 +$$
$$+ 1{,}644 \cdot 10^{-6} = -3{,}32 + 1{,}644 \cdot 10^{-6};$$
$$a_{45} = 1 - 0{,}25 \cdot 2{,}36 + 0{,}25 \cdot 1 = 1 - 0{,}59 + 0{,}25 = 0{,}66;$$
$$a_{55} = 1 + 0{,}25 \cdot 2{,}36 - 0{,}25 \cdot 1 = 1 + 0{,}59 - 0{,}25 = 1{,}34;$$
$$a_{16} = 6 - 2(-2 \cdot 2{,}36 + 1 + 3{,}72) - 2 \cdot 1{,}644 \cdot 10^{-6} = 6 - 3{,}288 \cdot 10^{-6};$$
$$a_{26} = -4 + 0{,}5(3{,}72 - 1) - 2 \cdot 2{,}36 + 1 + 3{,}72 + 1{,}644 \cdot 10^{-6} = -4 - 1{,}36 - 4{,}72 +$$
$$+ 4{,}72 + 1{,}644 \cdot 10^{-6} = -2{,}64 + 1{,}644 \cdot 10^{-6};$$
$$a_{36} = -4 - 1{,}36 - 4{,}72 + 4{,}72 + 1{,}644 \cdot 10^{-6} = -5{,}36 + 1{,}644 \cdot 10^{-6};$$
$$a_{46} = 1 - 0{,}25 \cdot 3{,}72 + 0{,}25 \cdot 1 = 1 - 0{,}9305 + 0{,}25 = 0{,}3195;$$
$$a_{56} = 1 + 0{,}25 \cdot 3{,}72 - 0{,}25 \cdot 1 = 1 + 0{,}9305 - 0{,}25 = 1{,}6805;$$
$$a_{17} = 6 - 2(-2 \cdot 3{,}72 + 2{,}36 + 3{,}72) - 2 \cdot 1{,}644 \cdot 10^{-6} = 6 + 2{,}72 - 3{,}2844 \cdot 10^{-6} =$$
$$= 8{,}72 - 3{,}2844 \cdot 10;$$
$$a_{27} = -4 + 0{,}5(3{,}72 - 2{,}36) - 2 \cdot 3{,}72 + 3{,}72 + 3{,}72 + 2{,}36 + 1{,}644 \cdot 10^{-6} =$$
$$= -4 + 0{,}68 - 7{,}44 + 3{,}72 + 2{,}36 + 1{,}644 \cdot 10^{-6} = -4{,}68 + 1{,}644 \cdot 10^{-6};$$
$$a_{37} = -4 - 0{,}68 - 7{,}44 + 3{,}72 + 2{,}36 + 1{,}644 \cdot 10^{-6} = -6{,}04 + 1{,}644 \cdot 10^{-6};$$
$$a_{47} = 1 - 0{,}25 \cdot 3{,}72 + 0{,}25 \cdot 2{,}36 = 1 - 0{,}93 + 0{,}59 = 0{,}66;$$
$$a_{57} = 1 + 0{,}25 \cdot 3{,}72 - 0{,}25 \cdot 2{,}36 = 1 + 0{,}93 - 0{,}59 = 1{,}34;$$
$$a_{18} = 6 - 2(-2 \cdot 3{,}72 + 3{,}72 + 3{,}72) - 2 \cdot 1{,}644 \cdot 10^{-6} = 6 - 3{,}2844 \cdot 10^{-6};$$
$$a_{28} = -4 + 0{,}5(3{,}72 - 3{,}72) - 2 \cdot 3{,}72 + 3{,}72 + 3{,}72 + 1{,}644 \cdot 10^{-6} = -4 + 1{,}644 \cdot 10^{-6};$$
$$a_{38} = -4 - 0{,}5(3{,}72 - 3{,}72) - 2 \cdot 3{,}72 + 3{,}72 + 3{,}72 + 1{,}644 \cdot 10^{-6} = -4 + 1{,}644 \cdot 10^{-6};$$
$$a_{48} = 1 - 0{,}25 \cdot 3{,}72 + 0{,}25 \cdot 3{,}72 = 1; \quad a_{58} = 1 + 0{,}25 \cdot 3{,}72 - 0{,}25 \cdot 3{,}72 = 1.$$

2. Conclusions

1) This article deals with studying operation of metal panel with an opening used as machine parts (Figure 1).

2) In order to simplify the calculations and bring it to the applied (engineering) technique, the initial panel is replaced with a conventional (equivalent) stepwise-variable rigidity rod loaded with vertical and horizontal load (Figure 2).

3) Studying stress-strain state of such an equivalent rod is performed by the numerical finite difference (FDM) method using a linear grid (the number of computed nodes is eight, Figure 2).

4) On the basis of FDM there has been obtained the resolving matrix "A" in a general (alphabetic) form (Table 1) which permits to design of various panels with openings for different geometric sizes and values of external load.

5) With the use of computers there have been made all the needed calculations and obtained the diagrams of the power and strain state of the rod (Figure 5) which make it possible to evaluate strength, rigidity, and stability of the panels with an assessment of their operational reliability.

6) Reliability of the obtained results is confirmed by the correct coincidence of the ordinates of the M, Q, N diagrams with their corresponding values calculated by the classical theory of strength of materials (analytical method).

7) Thus, approximation (replacement) of operation of a two-dimensional isotropic panel with openings (Figure 1) equivalent in the longitudinal and flexural rigidity of a one-dimensional rod with stepwise-variable rigidity (Figure 2) gives acceptable from the standpoint of engineering accuracy results and greatly simplifies the procedure of designing wall panels.

8) The theoretical provisions and applied results given in this work can be used in engineering practice of designing parts and structures of machines and mechanisms.

References

[1] Varvak P.M., Varvak L.P. Method of grids in problems of calculating building structures. – M.: Stroyizdat, 1977. – 154 p.
[2] Weinberg D.V. Reference book on Strength, Stability and Oscillations of Plates. - Kiev: Budivelnik, 1973. - 328 p.
[3] Reference book on theory of elasticity; Ed. P.M. Varvak, A.F. Rebov. - Kiev: Budivelnik, 1971. - 613 p.
[4] Akhmediev S.K., Filippova T.S., Oryntayeva G.Zh., Donenbayev B.S. Analytical and numerical methods for calculating engineering and transport structures. - Karaganda: KSTU, 2016. - 158 p.
[5] Alfutov N.A. Basics of calculating stability of elastic circuits. – M.: Mechanical Engineering, 1978. - 311 p.
[6] Reference book of industrial, residential and public buildings and structures designer. Design-and-theoretical, in 2 books. Books 1, 2; Ed. Umansky A.A. – M.: Stroyizdat, 1973. – 600 p. book 1, - 625 p. book 2.
[7] Timoshenko S.P., Goodyer D.Zh. Theory of elasticity. – M.: Nauka (Fizmatgiz), 1975. - 576 p.

Information of the authors

Akhmediev Serik Kabultaevich, candidate of technical sciences, professor of the department of mechanics of Karaganda Technical University
E-mail: s.ahmediev@kstu.kz

Filippova Tatyana Silinyevna, candidate of technical science, professor of the mechanics department of Karaganda Technical University
E-mail: confucius_kstu@mail.ru

Oryntayeva Gulzhaukhar Zhunuskanovna, senior lecturer of the mechanics department of Karaganda Technical University
E-mail: oryntaeva70@mail.ru

Donenbaev Bakhytzhan Serikovich., PhD, senior lecturer of the mechanics department of Karaganda Technical University
E-mail: bahytshan09@mail.ru

DOI 1052209/2706_977X_2021_4_29 **IRSTI 53.49.15** **UDC 669.715**

The Joint Effect of Zr and Sc Small Additions on Electrical and Mechanical Properties of Pure Aluminum

Belov N.A.*
National Research and Technological University "MIS&A", Moscow, Russia
*corresponding author

Abstract. The joint effect of Zr and Sc additions on structure, electrical resistivity, mechanical properties and thermal stability of cold rolled sheets of pure aluminum has been studied. Foundry flat ingots (thickness of 15 mm) were rolled in two variants: (1) without any intermediary annealing, (2) using an intermediary annealing. Sheets (final thickness of 0.7 mm) were annealed at 300 °C and held for 1 up to 500 h. To calculate the liquidus temperatures, the solubilities of Zr and Sc in aluminium solid solution-(Al) and volume fractions of L12 nanoparticles (Al_3Zr, Al_3Sc and $Al_3(Zr,Sc)$), the *Thermo-Calc* software was used. It was found that all 3 alloys have the unrecrystallized structure after annealing (including 500 h holding). The size of subgrains is about 1 μm while the average size of $L1_2$ precipitates doesn't exceed 10-15 nm. The value of combination of various properties was estimated using the desirability function (D), which makes it possible to change characteristics with different dimensions into dimensionless values within the range of 0 to 1. It was shown that the alloy Al–0.24%Zr–0.1%Sc has the best value of D comparing with binary alloys and pure aluminium.

Keywords: Al-Zr-Sc alloys, Al3(Zr,Sc) nanoparticles, electrical resistivity, strength

Introduction

During last days in the different areas of electro-technical industry there is increased interest to the thermal stable aluminium alloys that should combine high electrical conductivity and sufficient strength which remains after heating up to 300 °C. The most prospective alloys for this application are low-alloyed alloys with zirconium addition [1-4]. In particular such alloys are used for manufacture of wire for high-voltage lines cables. The greatest effect from zirconium addition is reached under condition of complete bonding of this element in nano-particles of metastable phase Al_3Zr that has L12 structure [1, 3]. The same particles are formed when scandium is introduced [5].

As soon as phases Al_3Zr and Al_3Sc are isomorphous, these two elements are often introduced together. In the last case the formula of L12 is usually noted as Al3 (Zr,Sc) [6-11]. In the paper [12] basing on ingots example it was shown that the most hardening effect in Al-Zr system is reached at ~0.6 % Zr, and in Al-Sc system an optimal concentration of scandium is about 0.3 %. Scandium is much more expensive than zirconium, but from the other side, introduction of the last element requests increased melting and casting temperatures. In alloys of Al-Sc system precipitation of L12 phase is forming quicker however they coarsen under heating over than 350 °C (i.e. their thermal shock is lower that alloys with zirconium addition have). The most successful combination of strength, adaptability, production cost and thermal shock is reached in ternary alloys, as was shown basing on example of Al-0.2%Zr-0.1%Sc composition [12]. Dependency of electrical characteristics from ratio between zirconium and scandium is not enough investigated. Only heat treatment regime has influence on strengthening of ingots, but in wrought products the number of factors is considerably increasing and this requests special investigation. Therefore the main target of the current paper was to study the influence of parameters of strain-thermal treatment on strength, electrical resistance and thermal stability of cold-rolled sheets of three typical alloys of Al–Zr–Sc system.

1. Experimental methods

The main subjects of study were sheets of three Al–Zr–Sc alloys produced from flat ingots (15×30×180 mm). The ingots were prepared from high-purity primary aluminium (99.99 %); zirconium and scandium were introduced as an Al–3.5%Zr and Al–2%Sc master alloys. The chemical composition of specimens (Table 1) was analyzed at an ARL 3560B-1583 emission spectrometer. Foundry ingots were cold-rolled on a laboratory rolling mill to a final sheet thickness of 0.7 mm in two variants: (F) without any intermediary annealing, (T) using an intermediary annealing at a rolling thickness of 4.3 mm by the regimes: 300 °C, 8 h for alloy 30 Sc and 300 °C, 8 h+450 °C, 8 h for Zr-containing alloys. Sheets were annealed at 300 °C and held for 1 up to 500 h (Table 2). Intermediate and final annealing of sheets was done in a Nabeltherm electric muffle furnace at a temperature maintenance accuracy within the limits of ±2 °C.

The mechanical properties of sheets (ultimate tensile strength - UTS, yield strength – YS, and relative elongation El at room temperature) were determined by the results of uniaxial tension tests on a Zwick Z250 testing machine. The specific electrical resistance (r) of sheet specimens of a given size was measured using a GW INSTEK GOM-2 digital programmable milliohmmeter. The operating principle of the instrument is based on measuring a voltage drop by a digital voltmeter across a measured resistor at the flow of a calibrated value of current through it. The rated length of sheet specimens was 100 mm. Metallographic studies were carried out using an Axiovert 200 MMAT light microscope and a JSM-35CF scanning electron microscope (LM and SEM, respectively). Sections cut from ingots and sheets (central parts) served as subjects of study. Sections were prepared using both mechanical (Struers Labopol-5) and electrolytic polishing, as these two methods complement each other to give a more complete

idea of the microstructure. An electron probe microanalysis (EPMA) was also done at the JSM-35CF microscope using a wave spectrometer. The fine structure (primarily, of nanoparticles of the Zr-containing phase) was studied on a JEM2100 transmission electron microscope at an accelerating voltage of 200 kV (TEM). To calculate the liquidus temperature, the solubilities of zirconium and scandium in aluminium solid solution ($C_{(Al)}$), and volume fraction (Qv) of nanoparticles of L12 phase the Thermo-Calc software (database TTAL5) was used.

Table 1 - The chemical composition of experimental alloys and calculated values of the liquidus

No of alloy	Concentrations, wt.% (at.%)			T_L, $^0C^1$
	Zr	Sc	Zr+Sc	
1	0.64 (0.19)	0 (0)	0.64 (0.19)	836
2	0 (0)	0.30 (0.18)	0.30 (0.18)	660
3	0.24 (0.07)	0.10 (0.06)	0.34 (0.13)	741

[1]The liquidus temperature (calculation with Thermo–Calc software)

Table2 - Regimes of cold rolling (CR) and annealing of experimental alloys

Designation	Stages
F-0	CR (ε~95 %), no any heating
F-1	CR (ε~95 %)+300 °C, 1 h
F-10	CR (ε~95 %)+300 °C, 10 h
F-100	CR (ε~95 %)+300 °C, 100 h
F-500	CR (ε~95 %)+300 °C, 500 h
T-0	CR (ε~71 %)+300 °C, 8 h+450 °C, 8 h+ CR (ε~83 %)
T-1	CR (ε~71 %)+300 °C, 8 h+450 °C, 8 h+ CR (ε~83 %)+300 °C, 1 h
T-10	CR (ε~71 %)+300 °C, 8 h+450 °C, 8 h+ CR (ε~83 %)+300 °C, 10 h
T-100	CR (ε~71 %)+300 °C, 8 h+450 °C, 8 h+ CR (ε~83 %)+300 °C, 100 h
T-500	CR (ε~71 %)+300 °C, 8 h+450 °C, 8 h+ CR (ε~83 %)+300 °C, 500 h

The phase diagram Al-Zr-Sc was analyzed by way of calculations in order to choose optimal casting temperature that should wittingly exceed liquidus temperature (T_L). According to calculation (Table 1) a typical temperature (720 °C) for majority of commercial aluminum alloys is too low for the experimental compositions 1 and 3. And for alloy 1 even 800 °C is not enough, because corresponding value of T_L is 836 °C. Therefore, this alloy was prepared and casted at ~900 °C, in order to guarantee receipt of single-phase structure. Alloys 2 and 3 were prepared under considerable lower temperatures (720 and 780 °C accordingly), as they have more lower values of T_L.

2. Results and Discussion

Having approximately the same structure in as-cast state (single-phased) all three experimental alloys and pure aluminum didn't have difference in structure after rolling: all had fiber structure. Comparison of strength properties of sheets received according technological scheme (F) shows weak distinction between them. In particular, yield strength is at the level 150 MPa (Fig. 1a), i.e. a little bit higher that unalloyed aluminum has. It can be explained by the following: small additions of zirconium and scandium, which completely enter in (Al), lead to very insignificant solid-solution strengthening [12] and have weak influence on strain hardening. Second scheme (T) leaded to the more significant distinction in YS values (from 190 to 230 MPa), as shown at Fig. 1b. This result can be connected with some difference in Q_V values (Table 3) and different degree of decomposition of (Al) during process of intermediate annealing.

Significant distinctions were observing already after 1-hour intermediate annealing at 300 °C. Values of YS of alloys 1 and 2, manufactured according first scheme (F), are considerably differs. The strength of the first one stays at the initial level, but the second alloy reveals strong strengthening (approximately by 60 %). This explained by that scandium has more high diffusion in (Al), therefore decomposition of (Al) happens much faster. Note should be taken that the given temperature is an optimal for the precipitation hardening of alloys with scandium but too low for Al–Zr alloys [5]. When holding time is increased up to 500 h, the difference between these alloys is decreasing. For the first scheme it is connected with that alloy 1 is a little bit strengthening and alloy 2, on the contrary, softening (Fig. 2a). For the both schemes ternary alloy 3 demonstrates high stability: yield strength changes insignificantly in comparison with an initial level. As a whole, thermo-stability of all three alloys is much more than pure aluminum has, whose YS value after 1-hour annealing at 300 °C drops till 20 MPa.

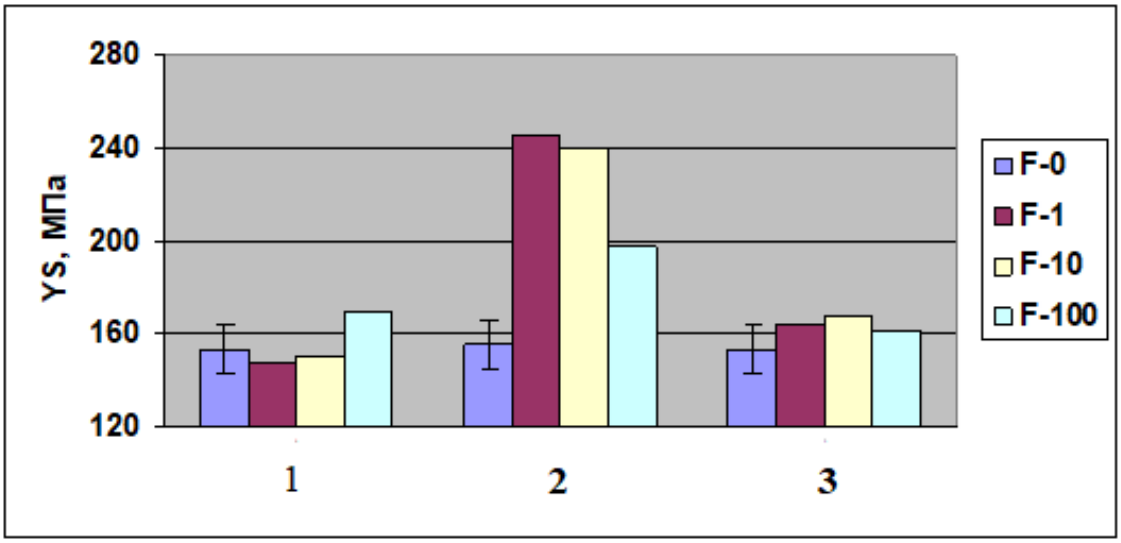

a)

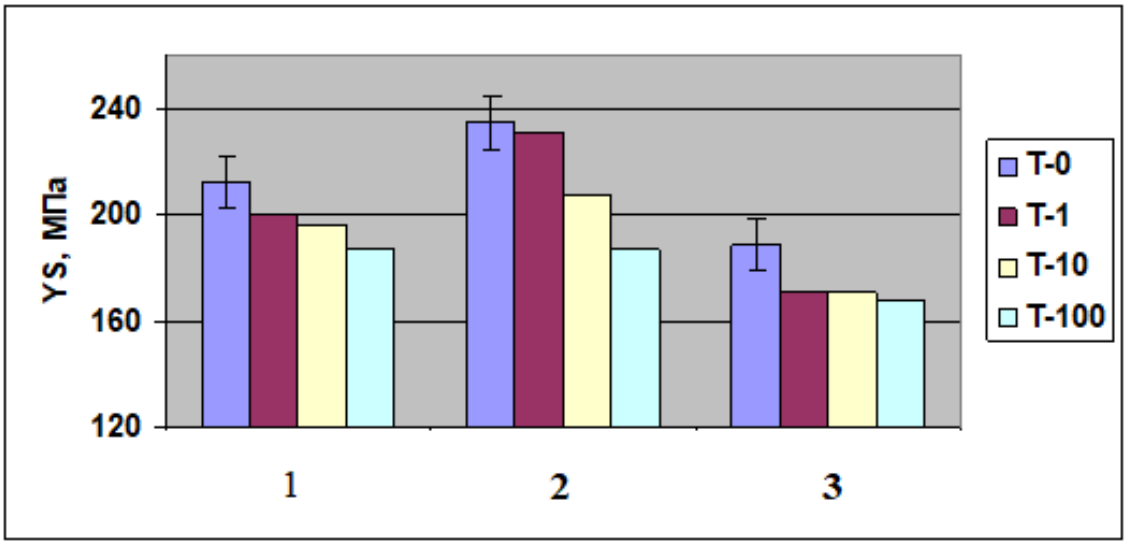

b)

a) scheme F; b) scheme T (see in Table 2)

Fig.1. - Yield strength (YS) of cold–rolled aluminum sheets versus annealing time at 300 ^{0}C for 1 up to 500 h

Table 3 - Calculated values of volume fraction of $L1_2$ phase and content of zirconium and scandium in aluminum solid solution

Alloy (see in Table 1)	Q_V, vol.%		$C_{(Al)}$, wt.% (at.%)			
	300 ^{0}C	450 ^{0}C	300 ^{0}C		450 ^{0}C	
			Zr	Sc	Zr	Sc
1	0.74	0.54	0.037(0.011)	–	0.204 (0.060)	–
2	0.72	0.65	–	0.004 (0.002)	–	0.046 (0.028)
3	0.52	0.38	0.018 (0.005)	0.002 (0.001)	0.088 (0.026)	0.026 (0.016)

[1]T_L–liquidus temperature; [2]Q_V–volume fraction of $L1_2$ phase at 300 °C; [3]C_Z and

Deformation-thermal regime of treatment has significant influence on the electrical resistivity (ρ), as shown at Fig. 2. As it was expected, maximum values of ρ of all three alloys are observed in F-0 state, so far as the maximum

concentration of alloying elements in (Al) corresponds to exactly this state. Annealing leads to the monotonous decreasing of electrical resistivity which is obviously connected with decomposition of (Al). Especially strong changes are observed in case of the first scheme (Fig. 2a). In particular, ρ value of alloy 2 during process of 500-hour annealing decreasing by 5.5×10-9 Ωm·×m. Intermediate annealing of the sheets (scheme T) significantly levels influence of holding (Fig. 2b). This is particularly noticeable for alloy 3, where difference of ρ values in T-0 and T-500 states doesn't exceed 0.5×10-9 Ωm·×m.

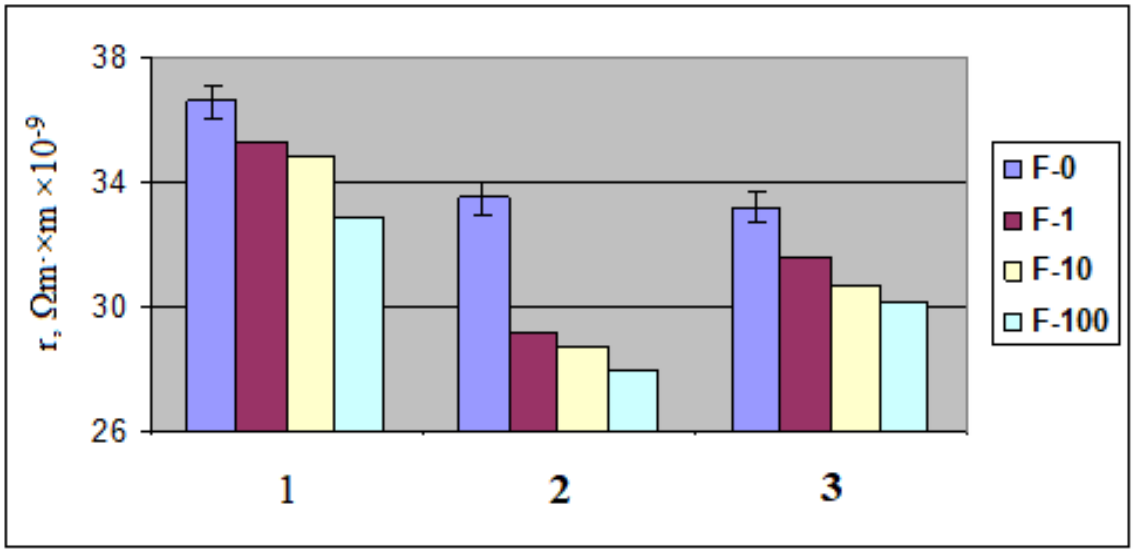

a)

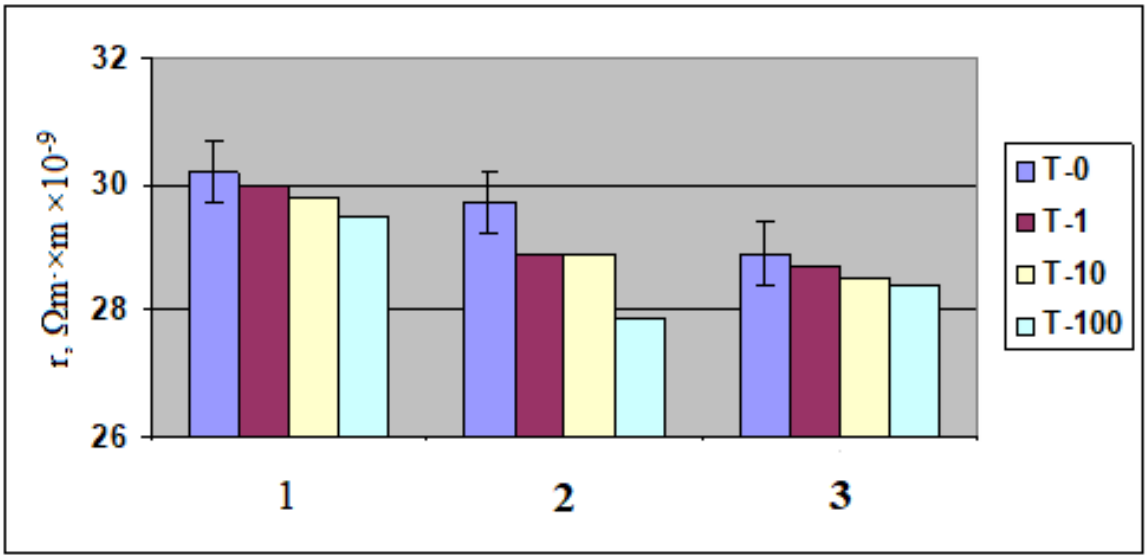

b)

a) scheme F; b) scheme T

Fig.2. - Electrical resistivity (ρ) of cold–rolled aluminium sheets (64 Zr, 30Sc and 24Zr10Sc alloys) versus annealing time at 300 oC for 1 up to 500 h

At Fig. 3a the light-field picture of polygonized substructure of ternary alloy is given. At the dark-field picture received in reflex 001 of phase $Al_3(Sc,Zr)$ it is seen that particles of precipitations of this phase have size of 10-15 nm and quite uniformly spread inside the sub-grain (Fig. 3b). There is no primary distribution of the particles of the second phase along sub-grains borders. At Fig. 3c picture of the particle of second phase received in high resolution is given. Mutual location of atom planes of the particle and matrix coincides, therefore lattices are coherent.

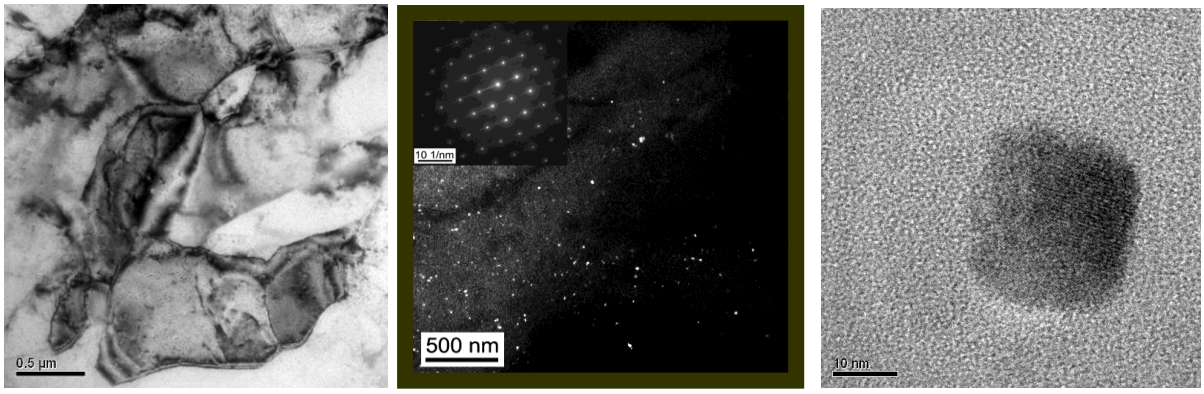

a) b) c)

a) polygonized substructure; b),c) nanoparticles of phase $Al_3(Sc,Zr)$

Fig.3. - TEM–structure of alloy 3 after holding at 300 °C during 500 hours

It is well known that in general case factors that lead to the alloy strengthening, increase ρ value, therefore the target of the maximum increasing of YS and saving of ρ level, is not simple [1-4]. However results achieved in current paper show more complicated ratio between ρ and YS (Fig. 1,2). In particular, alloys containing zirconium, manufactured according scheme F, demonstrate the contrary tendency: decreasing of ρ while YS is growing. This is connected with that the annealing of sheets at 300 °C lead to the formation of strengthening nano-particles of L12 phase and accompanying depletion of solid solution. The first factor is the reason of ρ decreasing and second – growing of YS. In 30Sc alloy decomposition happens so fast that increased electrical resistance observed only in work harded sheet manufactures according scheme F.

The best combination of various properties was estimated using the desirability function (D), which makes it possible to change characteristics with different dimensions into dimensionless values within the range of 0 to 1 [13]. The sought-for value of D is determined as a geometric mean of the desirability of separate properties (di). We considered three basic properties: 1, the specific electrical resistance in the initial state (ρ^{20}); 2, the yield strength in the initial state (YS); 3, the yield strength after a 1-h annealing at 300 °C (YS^{300}). Results adduced in Table 4, show that greatest values of D of all three alloys are reached when technological scheme T is realized. All of them in this state are much more exceed pure aluminum because thermal stability of the last one is very low (1-hour heating of sheets lead to the full recrystallization). The basic lack of scheme F is obviously consists in increased value of ρ, that stipulates low value of corresponding desirability (d_1). The ternary alloy 3 in state T has the best value of D comparing with binary alloys and pure aluminium.

Table 4 - Initial data for calculation of desirability function (D)

Alloy[1]	Scheme[2]	ρ^{20}, $\Omega m \cdot \times m \cdot 10^{-9}$	YS, MPa	YS^{300}, VLa	D	d1	d2	d3
Al (99,99)	F	27,2	128	13	0,26	0,75	0,33	0,07
1	F	36,6	147	150	0,07	0,00	0,39	0,47
	T	30,2	212	200	0,55	0,46	0,59	0,62
2	F	33,5	155	245	0,31	0,10	0,42	0,73
	T	29,7	235	231	0,62	0,52	0,66	0,69
3	F	33,2	153	163	0,30	0,12	0,41	0,51
	T	28,9	189	171	0,56	0,61	0,53	0,53
Reference values		31	140	120	0,37	0,37	0,37	0,37
		28	250	230	0,7	0,7	0,7	0,7

[1] see in Table 1, [2] see in Table 2

3. Conclusions

1) Influence of parameters of deformation and thermal treatment on strength (YS), specific electrical resistance (ρ) and thermal stability of cold rolled sheets of three aluminum alloys with zirconium and scandium additions (0.64 % Zr, 0.3 % Sc, and 0.24 % Zr+0.10 % Sc) was investigated.

2) The additions of zirconium and scandium are significantly increase ρ value, which is possible to decrease by application of annealing. Parameters of annealing have to be chosen proceeding from ultimate concentration of Zr and Sc in (Al) and rate of decomposition of the last one.

3) All experimental alloys have high thermal stability to the heating at 300 °C, what stipulated by resistance of nano-particles of L12 phase (Al_3Zr, Al_3Sc and $Al_3(Zr,Sc)$) to the coarsening up to 500 hours.

4) By the use of desirability function it is shown that ternary alloy has the best combination of strength, electrical resistivity and thermal stability.

References

[1] Belov N.A., Alabin A.N., Matveeva I.A., Eskin D.G. Effect of Zr additions and annealing temperature on electrical conductivity and hardness of hot rolled Al sheets //Trans. Nonferrous Met. Soc. China, 25, 2015. – P. 2817–2826. doi:10.1016/S1003-6326(15)63907-3.

[2] Knych T., Piwowarska M., Uliasz P. Studies on the process of heat treatment of conductive AlZr alloys obtained in various productive processes //Arch. Metal. Mater., 56, 2011. – P. 687–692. doi:10.2478/v10172-011-0075-z.

[3] Orlova T.S., Mavlyutov A.M., Latynina T.A., Ubyivovk E.V., Murashkin M.Yu., Schneider R., Gerthsen D., Valiev R.Z. Influence of severe plastic deformation on microstructure strength and electrical conductivity of aged Al-0.4Zr (wt.%) alloy //Rev. Adv. Mater. Sci., 55, 2018. – P. 92–101. doi:10.1515/rams-2018-0032.

[4] Çadırl E., Tecer H., Sahin M., Yılmaz E.; Kırındı T., Gündüz, M. Effect of heat treatments on the microhardness and tensile strength of Al–0.25 wt.% Zr alloy. //J. Alloys Compd., 632, 2015. – P. 229–237. doi:10.1016/j.jallcom.2015.01.193.

[5] Costa S., Puga H., Barbosa J., Pinto A.M.P. The effect of Sc additions on the microstructure and age hardening behaviour of as cast Al–Sc alloys //Materials and Design, 42, 2012. – P. 347–352.

[6] Forbord B., Lefebvre W., Danoix F., Hallem H., Marthinsen K. Three dimensional atom probe investigation on the formation of Al3(Sc,Zr)-dispersoids in aluminium alloys //Sripta Mater., 51, 2004. – P. 333-337.

[7] Fuller C.B., Seidman D.N. Temporal evolution of the nanostructure of Al(Sc,Zr) alloys: Part II-coarsening of Al3(Sc1−xZrx) precipitates //Acta Mater., 53, 2005. – P. 5415–5428.

[8] Clouet E., Barbu A., Lae L., Martin G. Precipitation kinetics of Al_3Zr and Al_3Sc in aluminum alloys modeled with cluster dynamics //Acta Mater, 53, 2005. – P. 2313–2325.

[9] Knipling K.E., Karnesky R.A., Lee C.P., Dunand D.C., Seidman D.N. Precipitation evolution in Al–0.1Sc, Al–0.1Zr and Al–0.1Sc–0.1Zr (at.%) alloys during isochronal aging //Acta Mater., 58, 2010. – P. 5184–5195.

[10] Deschamp A. and Guyo P. In situ small-angle scattering study of the precipitation kinetics in an Al–Zr–Sc alloy //Acta Mater., 55, 2007. - P. 2775-2783.

[11] Lefebvre W., Danoix F., Hallem H., Forbord B., Bostel A., Marthinsen K. Precipitation kinetic of Al_3 (Sc,Zr) dispersoids in aluminium //J. of Alloys and Comp., 470, 2009. – P. 107–110.

[12] Belov N.A., Alabin A.N., Eskin D.G., Istomin-Kastrovskiy V.V. Optimization of hardening of Al–Zr–Sc cast alloys, J. Mater Sci., 41, 2006. – P. 5890-5899.

[13] Harrington E. The desirability function, Industrial quality control, 21, 1965. - P. 494-498.

Information of the authors

Belov Nikolay Alexandrovich, doctor of technical science, professor of Materials Science and Light Alloys of National Research and Technological University "MIS&A"
E-mail: nikolay-belov@yandex.ru

DOI 1052209/2706_977X_2021_4_35 **IRSTI 55.53.13** **UDC 656.073.235**

Studying the Method of Loading Containers by Testing in the Software Environment

Ibatov M.M., Balabaev O.T., Kassymzhanova A.D.*
Karaganda Technical University, Karaganda, Kazakhstan
*corresponding author

Abstract: Reporting a new method for loading and unloading ISO containers transporting by railways. The article presents the results of research work carried out in the field of transportation of the bulk cargo by rail. The stress and displacement distribution in the elements of a universal container are studied. The results of the construction of a computer three-dimensional model, which is a copy of the container, are presented. The research was carried out in the SolidWorks "Simulation" software environment. There was carried out the patent search in the field of loading the bulk cargo into containers transported by railway platforms. The dependence of the output indicators on the influencing factors has been obtained with the yield strength in the material of the fasteners: 620,39 MPa. The conclusion is that the presented results of experimental studies are of applied value and will be interesting for scientific and engineering workers.

Keywords: stationary hoist, railway platform, container loading, ISO container, bulk cargo.

Introduction

Kazakhstan is one of the six largest exporters of wheat in the world and annually on average sells 6 million tons of wheat for export. However, there are a number of problems for the sale of domestic wheat. The analysis carried out in this area [1, 2] shows that the main reason that hinders exporting Kazakh wheat to China and European countries is the difference in the railway track width.

Nowadays, Kazakhstan partially uses the technology of transportation on special platforms with a lowered center of gravity for transportation in two tiers, which will reduce the cost of container transportation by 30-50 %. However, how versatile are these containers and is it possible to use them in industrial plants and agriculture, in particular for the bulk cargo? The problem lies in the complexity of organization of complex mechanization of loading and unloading the containers.

Today, container transportation of the bulk cargo is poorly studied, that was the purpose of the joint research.

1. Results and discussion

At the same time, the most difficult in solving acute problems in this aspect is organization of loading and unloading operations in the course of transportation of the bulk cargo.

Today there is a known method that consists in the fact that the loading of containers is carried out directly on railway platforms, which are in a coupling between themselves along the overpasses, performing transport and reloading operations with a forklift.

«The disadvantage of this method is inability to load the bulk cargo into containers transported by railway platforms. Thus, this imperfection of the known methods leads to decreasing the efficiency of loading operations for containers transported by railway platforms» [3].

A united team of departments of technical universities completed the work at the development of a method for loading containers transported by railway platforms.

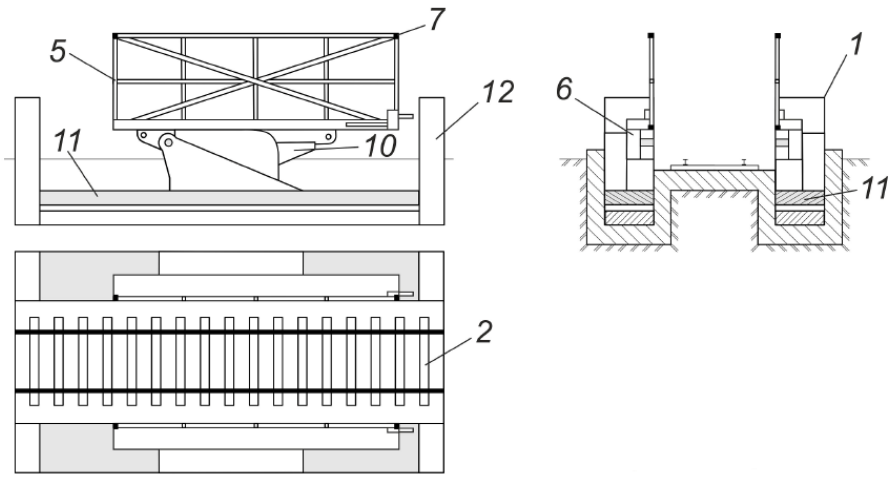

Fig. 1. – Stationary hoist

The developed method is illustrated in Figure 2 and consists of the following stages:

Hydraulic hoist 1 is mounted on railway track 2 under the hopper with the bulk cargo (Figure 1). Having received a signal to start loading operations, the shunting locomotive pushes railway platforms with empty containers along the way, so that container is placed between holders 5 of the hydraulic hoist. The holders of the hydraulic hoist squeeze (using horizontal-acting drives 6, Figure 1) the container on both sides, after which the container is fixed by the standard method using locks 7 (Figure 1) to the fittings. The devices for opening and closing doors are attached to container doors. Horizontal-acting drives and vertical-acting drives 10 (Figure 1) are located on platforms 11 (Figure 1). After fastening the container, elevating drives 12 (Figure 1) raise the platforms, and together they elevate the container to the height needed for the container rotation. Vertical-acting drives located on the platform begin to rotate the container and set it vertically on the end wall. On the container standing on the end wall, devices open the container doors to load the bulk cargo from the hopper. The bulk cargo is loaded from the hopper into the container. After the completion of loading the bulk cargo, devices close the container doors. There is performed the work described in the steps in reverse order. Depending on the number of railway platforms with containers, the described operations before are performed for each empty container. Having received a signal of the completion of loading operations, the shunting locomotive picks up the railway platforms with loaded containers on the way.

As a result of improving the method of loading containers transported by railroad platforms, a patent was obtained and was later published in the Derwent Innovations Index of Web of Science maintained by Clarivate Analytics [4].

To solve the research problems, such as assessing reliability, ensuring the safety of containers in the course of the grain cargo transportation, the SolidWorks software package was selected. In this environment, a computer three-dimensional model was built that was a copy of the container.

Below there are the used container model parameters:

1) Parameters of the universal container model:

- the overall dimensions are 6058 × 2438 × 2591 mm;
- the weight (net weight) is 2230 kg.

The material is plain carbon steel.

2) Parameters of the grain cargo model (wheat):

- the coefficient of internal friction of wheat 0.47-0.73);
- the coefficient of friction of wheat on steel 0.35-0.65;
- the bulk weight of wheat 0.7 - 0.83 t/m^3.

Improving the technological process of transporting wheat in containers is an urgent task and requires a detailed study and development of scientific and technical foundations of this aspect.

For theoretical and experimental studies, a standard 20-foot ISO container was selected. Its carrying capacity is 22 tons, the tare weight is 2.37 tons. At the 100 % filling of the container, the load on the elements of the locking devices will be 24.37 tons.

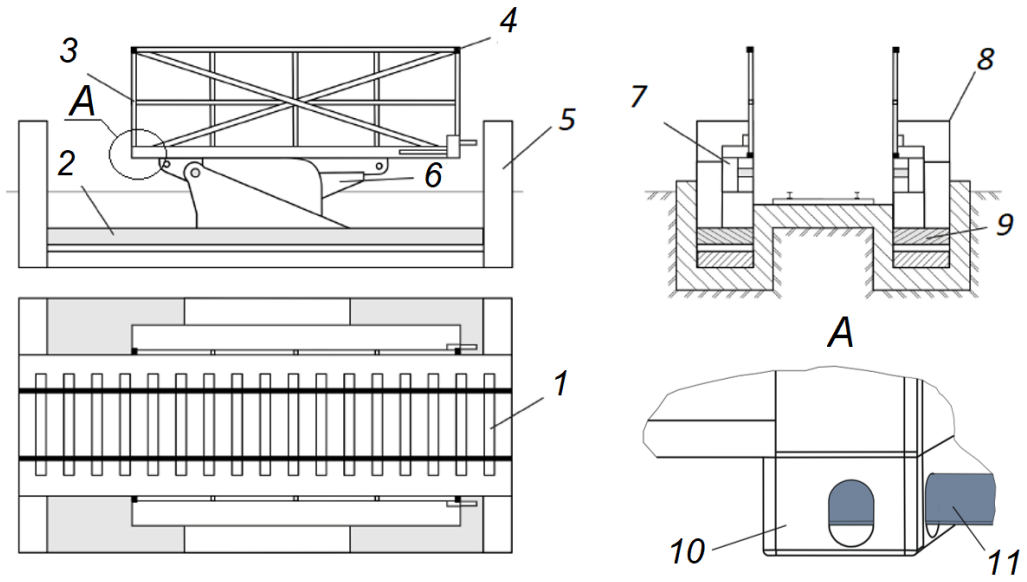

1 – railway track, 2 – platform, 3 – holders, 4 – locks, 5 – lifting drives, 6 – vertical-action drives, 7 – horizontal-action drives, 8 – hydraulic lift, 9 – platform, 10 – fitting, 11 – locking pin

Fig. 2. – Stationary hoist

For more accurate determining the design parameters of the stationary hoist design being developed, it is necessary to carry out detailed experimental studies in applied programs with developing 3D models of the main parts and assemblies. One of the first completed stages of this study is the developed methodology of determining the stress-strain state of the locking pin of the stationary hoist (hereinafter referred to as SHLP) [5]. This technique is based on experimental studies carried out in the SolidWorks "Simulation" software environment in the following order:

1) Establishing influencing factors and output indicators;
2) Selecting the number of tests;
3) Carrying out studies in the SolidWorks "Simulation" software environment.

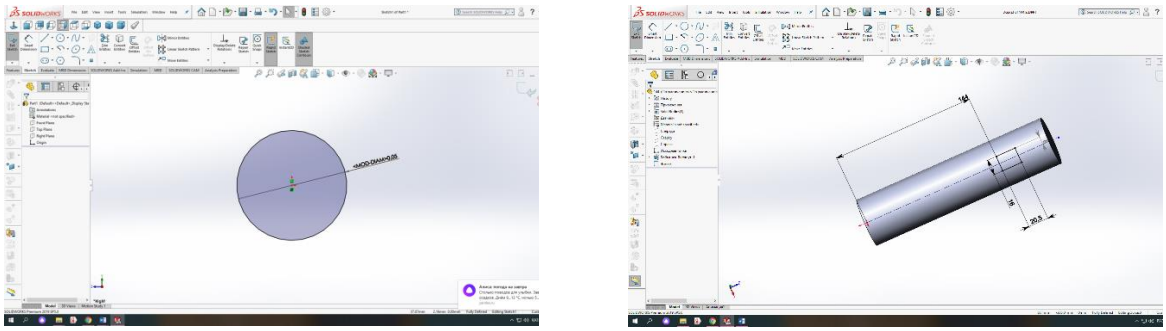

a) b)

Fig. 3. – Developing a 3D model of the SHLP design

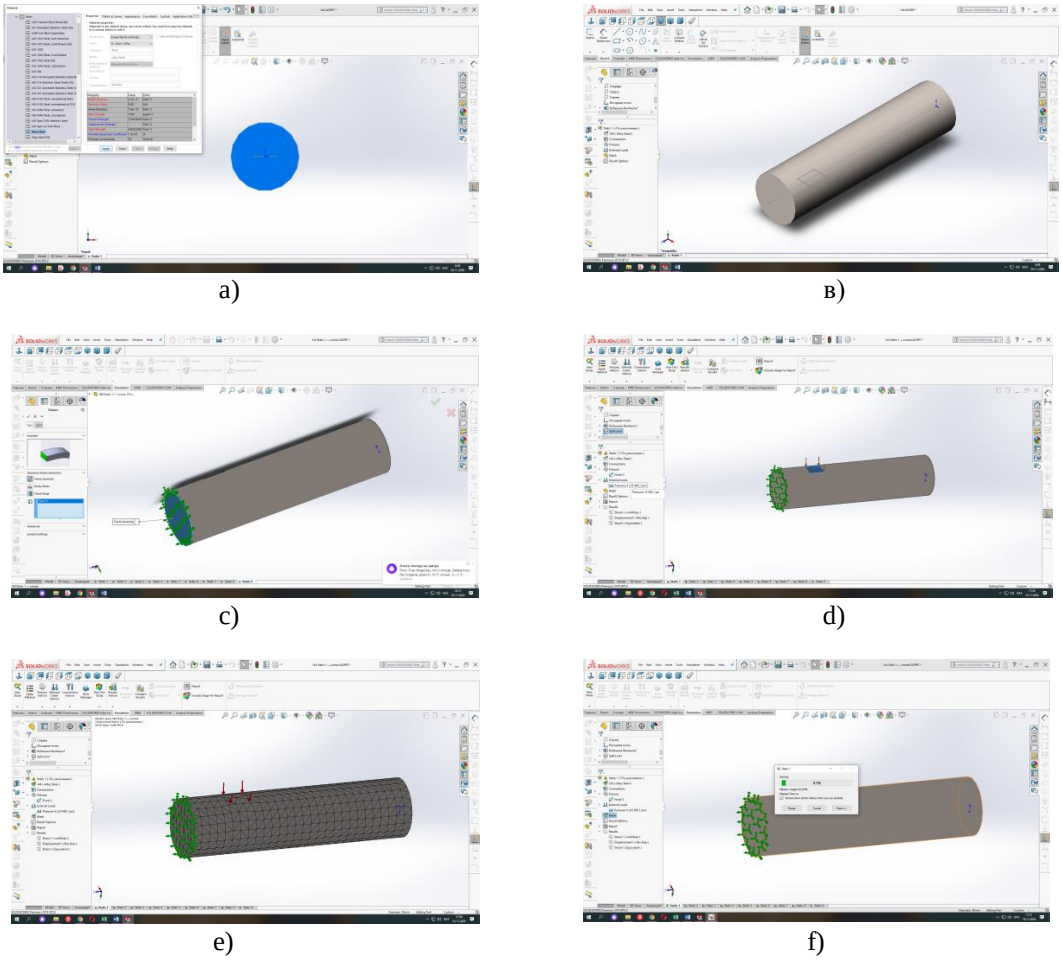

a) в)

c) d)

e) f)

Fig. 4. – Calculation the SHLP structure in the SolidWorks “Simulation” software environment

According to the results of tests carried out in the SolidWorks "Simulation" software environment, an experimental dependence (Figure 5) of mechanical stresses $\sigma_{\ni i}$ (MPa) in the material of the SHLP structure on the specified external force *Fi* (N) per area *S* (m^2) was obtained, with the yield point of 620.39 MPa.

The difference of experimental and theoretical results is shown in Figure 5. It can be seen from the calculation results (Table 1) performed with the use of empirical equation that the error does not exceed 15 %.

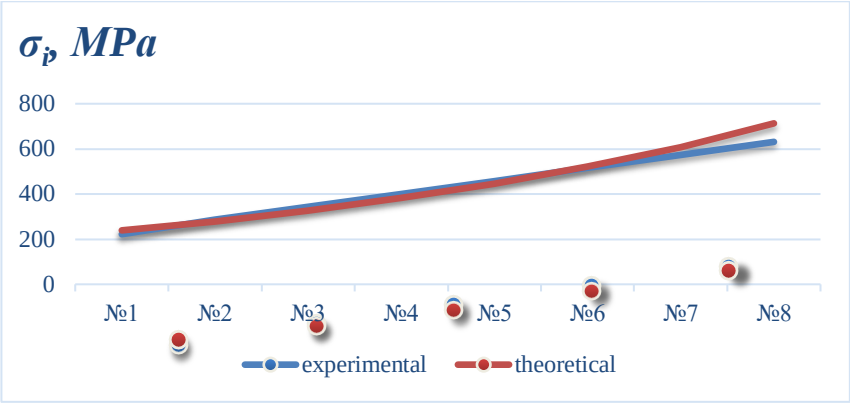

Fig. 5. – Comparison of experimental and theoretical results

Table 1 - Results of calculating studies mechanical stresses

Indicators	Tests							
	No.1	No.2	No.3	No.4	No.5	No.6	No.7	No.8
F_i/S, MPa	179	224	268	313	358	402	447	492
$\sigma_{эi}$, MPa	222	286	344	401	458	515	574	631
σ_{Ti}, MPa	239	278	326	383	446	522	608	713

2. Conclusions

The presented results lead to the following conclusions: an experimental study is of applied value and the developed method makes it possible to increase the efficiency of using ISO containers transported by railway platforms.

Also, for higher accuracy of determining the rational design parameters, detailed studies are required with the development of a digital model in the ANSYS application programs.

References

[1] Ibatov M.K., Ilessaliyev D.I., Kassymzhanova A.D. To the results of studying loading modes of universal containers. // Integration of science, education and production is the basis for the implementation of the Plan of the Nation (Saginov's Readings No. 12): Proceedings of the International Scientific and Practical Online Conference June 18-19, 2020 - Karaganda: KSTU Publishing House, 2020. Part 2. - P. 585-586.
[2] Ibatov M.K., Ilessaliyev D.I., Kassymzhanova A.D. To the Issue of Increasing LPI By Improving the Method of Loading Containers. University Proceedings., No. 3, 2020. - P. 94-96
[3] Kassymzhanova A.D., Balabayev O.T. Improving the way of loading containers transported by railway platforms. // Bulletin of ENU named after L.N. Gumilyov. Ser. Engineering science and technology, № 6, 2017. - P. 34-37.
[4] Vitvitskii E.E., Gumarov G.S., Balabaev O.T., Abishev K.K., Sarzhanov D.K., Kassymzhanova A.D. Method for loading bulk goods in containers transported by railway: Patent Number(s): RU2654439-C1 for invention // Derwent Primary Accession Number: 2018-53628L.
[5] Vitvitski E.E., Gumarov G.S., Balabayev O.T., Abishev K.K., Sarzhanov D.K., Kassymzhanova A.D. Method of loading bulk cargo into containers transported by railway platforms. // RF patent for invention No. 2654439. Published: 17.05.2018 Bul. No. 14.

Information of the authors

Ibatov Marat Kenesovich, Ibatov Marat Kenesovich, Doctor of Technical Sciences, Professor, Rector of Karaganda Technical University
E-mail: kstu@kstu.kz

Balabaev Oyum Temirgalievich, candidate of technical sciences associate professor of the Department of "Industrial Transport" of Karaganda Technical University
E-mail: balabaev.ot@mail.ru

Kasymzhanova Aidana Donenbaykyzy, teacher of the Department of "Industrial Transport" of Karaganda Technical University
E-mail: aidana_dak@mail.ru